Modelling the cosmic spectral energy distribution and extragalactic background light over all time

S. K. Andrews,[1,2]★ S. P. Driver,[1,2]★ L. J. M. Davies,[1] C. d. P. Lagos[1] and A. S. G. Robotham[1]

[1]*International Center for Radio Astronomy Research, The University of Western Australia, 35 Stirling Highway, Crawley, WA 6009, Australia*
[2]*School of Physics & Astronomy, University of St Andrews, North Haugh, St Andrews KY16 9SS, UK*

ABSTRACT

We present a phenomological model of the cosmic spectral energy distribution (CSED) and the integrated galactic light (IGL) over all cosmic time. This model, based on an earlier model by Driver et al., attributes the cosmic star formation history (CSFH) to two processes – first, chaotic clump accretion and major mergers, resulting in the early-time formation of bulges and secondly, cold gas accretion, resulting in late-time disc formation. Under the assumption of a Universal Chabrier initial mass function, we combine the Bruzual & Charlot stellar libraries, the Charlot & Fall dust attenuation prescription and template spectra for emission by dust and active galactic nuclei to predict the CSED – pre- and post-dust attenuation – and the IGL throughout cosmic time. The phenomological model, as constructed, adopts a number of basic axioms and empirical results and has minimal free parameters. We compare the model output, as well as predictions from the semi-analytic model GALFORM to recent estimates of the CSED out to $z = 1$. By construction, our empirical model reproduces the full energy output of the Universe from the ultraviolet to the far-infrared extremely well. We use the model to derive predictions of the stellar and dust mass densities, again finding good agreement. We find that GALFORM predicts the CSED for $z < 0.3$ in good agreement with the observations. This agreement becomes increasingly poor towards $z = 1$, when the model CSED is ∼50 per cent fainter. The latter is consistent with the model underpredicting the CSFH. As a consequence, GALFORM predicts a ∼30 per cent fainter IGL.

Key words: galaxies: evolution – galaxies: general – cosmic background radiation – cosmology: observations.

1 INTRODUCTION

One of the goals of modern cosmology is to understand, explain and predict the evolution of mass, energy and structure from the big bang to the present day. Here, we focus on the evolution of energy emanating from the ultraviolet to far-infrared wavelength range – photon production, transport and redistribution – over a 13 billion year timeline (i.e. since recombination). The energy content of the Universe over this wavelength range is often expressed through three measurable quantities: the cosmic spectral energy distribution (CSED) as a function of redshift, the extragalactic background light (EBL) and the integrated galactic light (IGL). These quantities are each measurable via distinct direct or indirect methods, but are also closely related. The CSED (e.g. Driver et al. 2008; Domínguez et al. 2011; Driver et al. 2016b; Andrews et al. 2017b) describes the

photons generated within a cosmologically representative volume at a specific epoch. The EBL can therefore be expressed as the volume and luminosity distance weighted integral of the redshifted CSED since decoupling. Hence, the EBL describes the distribution of photons observed today, originating from all post-decoupling processes from $\lambda_{obs} = 100$ nm to $\lambda_{obs} = 1$ mm. The IGL represents the dominant component of the EBL and is best derived from number counts of discrete resolved objects (e.g. galaxies and AGN) as observed by a sufficiently deep extragalactic survey (e.g. Driver et al. 2016c). In the absence of any diffuse light, the EBL and IGL will be identical – hence, any discrepancy between the two constrains the level of diffuse emission (Driver et al. 2016c).

The CSED, EBL and IGL encode statistical information about past and ongoing processes of photon production. The primary source of new photons at low and intermediate redshifts is from stellar nucleosynthesis. However, approximately half the photons being produced by stars are absorbed by dust in the host galaxy, which heats and re-radiates in the far-infrared (Savage & Mathis 1979;

Driver et al. 2008, 2016b; Andrews et al. 2017b). The remaining photons escape into the intergalactic medium. At higher redshifts, both components (direct and reprocessed photons) are supplemented by mass accretion on to active galactic nuclei (AGN) and their surrounding dust torii (e.g. Richards et al. 2006). Again, approximately half of the photons produced by AGN are also attenuated. However, in the AGN case the dust torus is significantly hotter and hence re-radiates at mid-infrared wavelengths. Remarkably, this approximate equality between optical and mid- to far-infrared energy output persists when integrating over all redshifts and is often divided into two distinct components – the cosmic infrared background (CIB, 8 μm < λ_{obs} < 1 mm in the observed frame; Dwek et al. 1998); and the cosmic optical background (COB, 0.1 μm < λ_{obs} < 8 μm), see e.g. Driver et al. (2016c).

Given the intimate link between the CSED, the EBL and galaxy evolution, it is insightful to obtain CSED and EBL predictions from semi-analytic (e.g. Gilmore et al. 2012; Somerville et al. 2012; Inoue et al. 2013) and phenomenological models (e.g. Partridge & Peebles 1967a,b; Finke, Razzaque & Dermer 2010; Driver et al. 2013; Khaire & Srianand 2015) of galaxy formation. Semi-analytic models, e.g. Lacey et al. (2016), begin with dark matter haloes as output from some *N*-body simulation (e.g. Springel et al. 2005), which accrete gas from the intergalactic medium according to a predefined prescription. The model determines the star formation history, metallicity evolution and feedback from supernovae and AGN from the accretion rate and the halo merger tree. The unattenuated spectral energy distribution (SED) can then be computed using stellar population synthesis codes (e.g. Bruzual & Charlot 2003; Maraston 2005), with dust attenuation and re-emission added via prescription.

Phenomological models are empirically driven and can be divided into two classes: forward modelling and backward modelling. Forward models (e.g. Driver et al. 2013) are based on measurements or assumptions of

(i) the cosmic star formation history (CSFH; e.g. Hopkins & Beacom 2006; Madau & Dickinson 2014);
(ii) stellar population synthesis (e.g. Bruzual & Charlot 2003; Maraston 2005);
(iii) a known Universal initial mass function (IMF);
(iv) the unattenuated SED of starlight; and
(v) a dust attenuation and emission model.

Backward modelling arises from evolving observed properties of nearby galaxies, for example luminosity functions (Franceschini, Rodighiero & Vaccari 2008) or the classification of galaxies by SED fitting (Domínguez et al. 2011), and propagating them backwards in time. Due to their simplistic design and high-level approach, phenomological models have fewer free parameters than approaches which look to encode galaxy physics and also recover clustering signatures – i.e. flexible but limited (phenomological) versus comprehensive but immutable (semi-analytic, hydrodynamic and *N*-body simulations).

Direct measurements of the COB (e.g. Matsumoto et al. 2005, 2015; Levenson & Wright 2008; Matsuoka et al. 2011; H.E.S.S. Collaboration 2013; Biteau & Williams 2015; Ahnen et al. 2016; Matsuura et al. 2017; Mattila et al. 2017; Zemcov et al. 2017) and CIB (e.g. Puget et al. 1996; Fixsen et al. 1998; Hauser et al. 1998) have been made using a number of different facilities and methods. Likewise, the IGL has been measured in the ultraviolet and optical (e.g. Madau & Pozzetti 2000; Totani et al. 2001; Xu et al. 2005; Keenan et al. 2010) to the mid- and far-infrared (e.g. Dole et al. 2006, Béthermin et al. 2012a;

Carniani et al. 2015), with some groups measuring how the CIB accumulates as a function of redshift at specific wavelengths (e.g. Chary & Elbaz 2001; Marsden et al. 2009; Berta et al. 2011; Jauzac et al. 2011; Béthermin et al. 2012b; Viero et al. 2013). These measurements are usually confined to a single facility and hence a narrow portion of the spectrum.

Robust measurements of the broader CSED have only recently become possible, as they rely on the availability of sufficiently deep and wide multiwavelength data. The first measurement of the dust corrected CSED and hence the far-infrared energy output was made by Driver et al. (2008) from existing optical luminosity density measurements. This measurement was updated by Driver et al. (2012), who integrated luminosity functions from FUV through *K* derived from the Galaxy and Mass Assembly (GAMA) survey. Domínguez et al. (2011) used a SED fitting code in order to interpolate between broad-band filters, Kelvin et al. (2014) examined the CSED as a function of galaxy morphology and Driver et al. (2016b) extended observations to the far-infrared. Finally, Andrews et al. (2017b) measured the CSED out to $z = 1$ based on a completely homogenous data reduction procedure across the entire ultraviolet to far-infrared wavelength range. In a similar vein, Driver et al. (2016c) computed the extrapolated IGL over the same wavelength range using consistent analysis techniques.

With this data now in hand, this work aims to both extend the Driver et al. (2013) forward model as well as derive a prediction of the CSED and IGL from the GALFORM semi-analytic model and compare each to the observations. In Section 2, we briefly recap our measurements of the IGL and CSED as reported by Driver et al. (2016c) and Andrews et al. (2017b), respectively. In Section 3, we revisit the Driver et al. (2013) model and extend it to include both dust attenuation and AGN. In Section 4, we derive predictions for both the unattenuated and attenuated CSEDs. In Section 5, we obtain predictions of the CSED from two recent incarnations of GALFORM. In Section 6, we compute a number of useful relationships from our phenomological model, including the integrated photon escape fraction (IPEF), the comoving IGL and the buildup of dust and stellar mass densities as predicted by our model. We conclude in Section 7.

We use AB magnitudes and assume $H_0 = 70h_{70}$ km s^{-1} Mpc^{-1}, $\Omega_\Lambda = 0.7$ and $\Omega_m = 0.3$ throughout.

2 EMPIRICAL ESTIMATES OF THE IGL AND CSED

The genesis of the IGL and CSED data we wish to reproduce is critical to our analysis, so we briefly describe how these data were derived below.

2.1 The integrated galactic light

In Driver et al. (2016c), we measured the IGL from a compendium of deep and wide galaxy number count data from the far-ultraviolet to the far-infrared. This included the GAMA (Wright et al. 2016a) and G10/COSMOS (Andrews et al. 2017a) data sets as well as a selection of deeper surveys, including data from the *Galaxy Evolution Explorer*, *Hubble*, *Spitzer*, *Wide-field Infrared Survey Explorer* and *Herschel* space telescopes. We found that the contributions to the IGL as a function of magnitude are bound at both bright and faint magnitudes for all bands. To determine the total energy in each band, we fitted a spline to the luminosity-weighted number count data and integrated it. Finally, to obtain a physically motivated IGL spectrum, we used a preliminary version of the model described

in this work. Summing our IGL spectrum over the relevant wavelength ranges, we found values for the COB and CIB of 24 ± 4 and 26 ± 5 nW m^{-2} sr^{-1}, respectively. These extrapolated IGL measurements agree well with previous literature IGL measurements, but fall significantly below the direct EBL estimates based on absolute background analysis of *Hubble* data (e.g. Bernstein, Freedman & Madore 2002). However, our IGL measurements, with a 20 per cent adjustment upward to account for intrahalo or intracluster light and low surface brightness galaxies, agree closely with the high-energy gamma-ray constraints from H.E.S.S. (H.E.S.S. Collaboration 2013) and MAGIC (Ahnen et al. 2016). Our measurements also agree with the direct EBL observations by the *Pioneer* and *New Horizons* spacecraft taken from the outer Solar system, where the impact of zodiacal light is much less significant (Matsuoka et al. 2011; Zemcov et al. 2017). This suggests that the direct measurements of the COB may have underestimated the terrestrial (Earthshine) and/or zodiacal contributions to the total sky background (see e.g. Kawara et al. 2017). In summary, the IGL measurements presented in Driver et al. (2016c) appear robust at all wavelengths with a tentative detection of diffuse light at the 0–20 per cent level in the near-infared.

2.2 The CSED as a function of redshift

While the EBL describes the total integrated light along the pathlength of the Universe, the (total) CSED represents its subdivision by redshift. In Andrews et al. (2017b), we measured the (resolved) CSED from the far-ultraviolet to the far-infrared over a 7.5 Gyr baseline using multiwavelength imagery and spectroscopy from the GAMA (Driver et al. 2011) and COSMOS (Scoville et al. 2007) surveys. The GAMA spectroscopic and imaging data are described in Liske et al. (2015) and Driver et al. (2016b) with photometry performed by Wright et al. (2016a), while the assembly of redshift and photometric data in the COSMOS region are described by Davies et al. (2015) and Andrews et al. (2017a), respectively.

The photometric measurements were then interpolated using the SED fitting code MAGPHYS (Multiwavelength Analysis of Galaxy Physical Properties; da Cunha et al. 2008) by Driver et al. (2017). As a reminder, the MAGPHYS fits use the Bruzual & Charlot (2003) stellar libraries based on a Chabrier (2003) IMF and the two component Charlot & Fall (2000) dust attenuation model. The resulting far-infrared dust emission spectrum comprises of polycyclic aromatic hydrocarbons, warm dust and two populations of cold dust in thermal equilibrium with varying temperatures. The resulting SED fits are generally robust, producing stellar mass and star formation rate estimates in line with independent estimates (Taylor et al. 2011; Davies et al. 2016, see also the direct comparison in Driver et al. 2017).

We stacked the MAGPHYS fits for individual galaxies in 10 redshift bins to derive both the unattenuated (dust corrected) and attenuated (observed) CSED for $0.02 < z < 0.99$. We found that the total energy output declined from $(5.1 \pm 1.0) \times 10^{35} h_{70}$ W Mpc^{-3} at $z = 0.905$ to $(1.3 \pm 0.3) \times 10^{35} h_{70}$ W Mpc^{-3} at the current epoch, a rate slightly slower than the well-known decline in cosmic star formation (Lilly et al. 1996) – as one would expect given that the CSED samples both young and old starlight. The quoted uncertainty in the absolute normalization of the CSEDs ranges from 11 to 27 per cent, and is dominated by cosmic sample variance. Additional, semiquantifiable and wavelength-dependent uncertainties arise from SED modelling error, incompleteness and the lack of complete far-infrared and ultraviolet measurements in G10/COSMOS. These are discussed in Andrews et al. (2017b), their fig. 6 and Section 3.3.

3 RECONSTRUCTING THE CSED

We now look to build a phenomological model of the CSED and elect to follow the pathway laid out in Driver et al. (2013) with the addition of AGN and a more comprehensive dust modelling prescription. To build our revised phenomological model of the energy output of the Universe, one needs:

(i) Empirical estimates of the CSFH (e.g. Hopkins & Beacom 2006; Madau & Dickinson 2014; Driver et al. 2017).

(ii) The assumption of a mean IMF across cosmic time (e.g. Kennicutt 1983; Kroupa 2001; Baldry & Glazebrook 2003; Chabrier 2003).

(iii) A stellar population model (e.g. Bruzual & Charlot 2003; Le Borgne et al. 2004; Maraston 2005).

(iv) A description of how the metallicity of newly formed stars evolves with redshift (Tremonti et al. 2004; Erb et al. 2006; Zahid, Kewley & Bresolin 2011 following Driver et al. 2013).

(v) A dust attenuation model (e.g. Cardelli, Clayton & Mathis 1989; Calzetti et al. 2000; Charlot & Fall 2000; Gordon et al. 2003) and corresponding emission spectra in the far-infrared (e.g. Chary & Elbaz 2001; Zubko, Dwek & Arendt 2004; Draine & Li 2007; Dale et al. 2014).

(vi) An emission model from AGN (e.g. Elvis et al. 1994; Dale et al. 2014; Siebenmorgen, Heymann & Efstathiou 2015) and either a prescription of linking that to the spheroid star formation rate, or some description of how AGN activity evolves with time (e.g. Richards et al. 2006; Palanque-Delabrouille et al. 2016).

Constructing a model in this manner should, in theory, require no tunable initial conditions – the choice of parameters in stellar, dust and AGN modelling should all be guided by empirical data. However, free parameters are unavoidable when the available data are insufficient to constrain the model. At the heart of the Driver et al. (2013) two-phase model there are two axioms, which we also adopt here:

(i) AGN activity traces stellar mass growth in spheroids.

(ii) The formation of material ending up in spheroids today dominates at high redshift.

The first axiom is based on the $M_{\rm bh}$–$M_{*,\rm sph}$ and $M_{\rm bh}$–σ relations (Magorrian et al. 1998; Gebhardt et al. 2000), which implies co-evolution between the central black hole and the surrounding spheroid (Silk & Rees 1998; Kormendy & Ho 2013; Graham & Scott 2015). However, while the $M_{\rm bh}$–$M_{*,\rm sph}$ relation is irrefutable, multiple studies have found no or only weak correlation between total (i.e. disc and spheroid) star formation and AGN activity (Mullaney et al. 2012a; Rosario et al. 2012; Stanley et al. 2015). At $z \lesssim 1.6$, we expect this to be the case as total star formation is dominated by cold gas accretion that never reaches the latent supermassive black hole (i.e. it is confined to discs only). This redshift corresponds to the transition point in the Driver et al. (2013) model. At $z \gtrsim 1.6$, we explicitly link *spheroid* star formation with AGN activity – both are associated with scenarios in which low angular momentum gas is driven towards the centre of the galaxy, fuelling a central starburst and black hole accretion. The lack of correlation at high redshift is therefore surprising. One possible solution is that these studies are either failing to separate bulge and disc star formation or mismatching time-scales. Instantaneous measurements may be affected by an AGN lag and/or the stochasticity of short-term star formation. When considering time-averaged AGN activity (as determined by X-ray stacking) and far-infared star formation measurements the correlation appears to strengthen (Mullaney et al. 2012b; Chen et al. 2013a; Rodighiero et al. 2015).
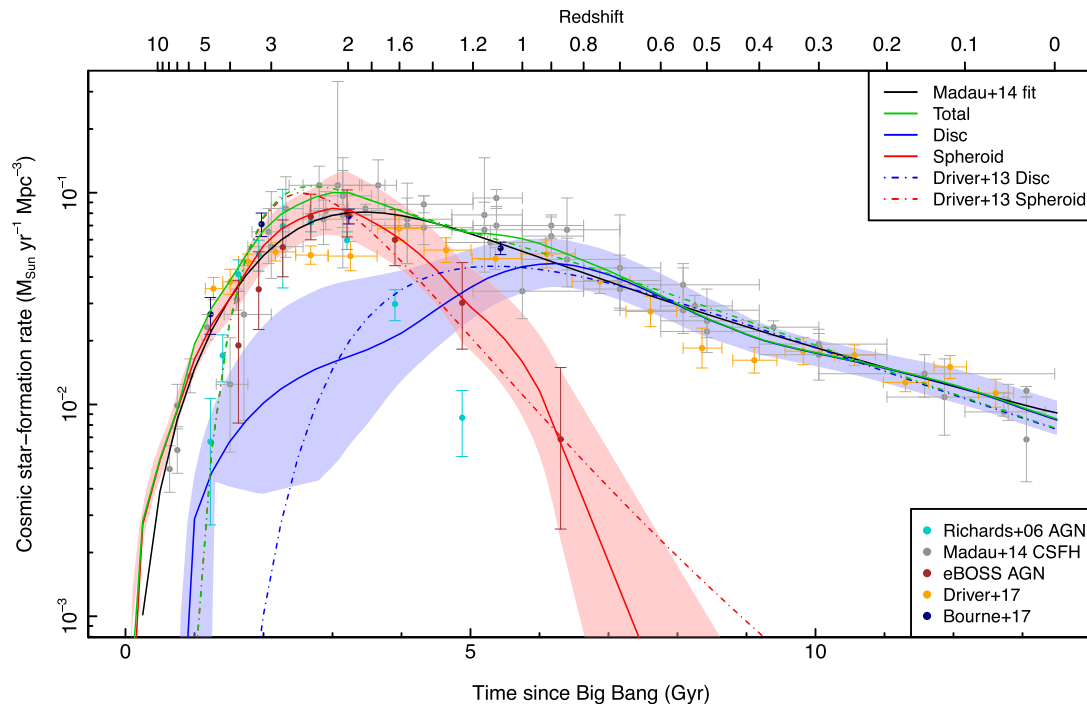
Figure 1. Our fitting functions to the CSFH for discs (blue), spheroids (red) and combined (green) compared to those for Driver et al. (2013) (dashed line) and Madau & Dickinson (2014) (solid black line). The corresponding error regions in the disc and spheroid CSFHs are also shown. The Madau & Dickinson (2014) CSFH data (grey points), the Driver et al. (2017) and Bourne et al. (2017) CSFH data (orange and dark blue points, respectively) and the Richards et al. (2006) AGN luminosity function data scaled to the Madau & Dickinson (2014) fitting function (red points) are also shown.

The case for the second axiom is stronger. The recent advent of integral field spectroscopic observations has enabled more robust determination of the mass growth history of galaxies. McDermid et al. (2015) found that early-type galaxies have formed 50 per cent of their stars by $z = 3$ and 90 per cent by $z \sim 0.9$. A similar picture is painted by Ibarra-Medel et al. (2016), with red, quiescent, high-mass and/or early-type galaxies forming a greater portion of their stars at higher redshifts. In both studies, low-mass galaxies undergo steady mass growth to the current epoch. González Delgado et al. (2015) showed that early-type galaxies contain older stellar populations (log (age) $\sim$ 9.5–10) than late-type galaxies (log (age) $\sim$ 8.5–9.5). Sa and Sb types show an older stellar population at low galactocentric radii, potentially corresponding to bulge material. Early-type and high-mass galaxies contain the majority of spheroid material in the Universe, while low-mass galaxies consist of predominantly disc material (e.g. Moffett et al. 2016a). This is consistent with the scenario we envisage in the two-phase model – spheroid star formation occurring primarily at higher redshifts, while star formation linked to cold gas accretion continues in low-mass galaxies and discs to the current epoch.

We proceed under the assumption that AGN activity is causally linked to, or coincidental with spheroid star formation on a time-averaged basis and now build up our model over five key stages:

(i) Compute the unattenuated CSED from the CSFH and an adopted gas-phase metallicity evolution.

(ii) Compute the attenuated CSED from a set of selected dust attenuation parameters, given the CSFH and metallicity evolution in stage 1.

(iii) Add far-infrared spectra based on the attenuated energy derived in stage 2.

(iv) Add AGN spectra based on the evolution of the AGN luminosity function with redshift.

(v) Construct the IGL from the full CSED as a function of redshift.

These ingredients are described below.

3.1 The cosmic star formation history

We take the opportunity to update the Driver et al. (2013) fitting functions of the CSFH as follows:

We replace the compilation of cosmic star formation rate measurements with that from Madau & Dickinson (2014) augmented by the recent measurements from Driver et al. (2017) and Bourne et al. (2017). We replace the Richards et al. (2006) AGN *i*-band total luminosity data with *g*-band (rest frame) data from the extended Baryon Oscillation Spectroscopic Survey (eBOSS; Palanque-Delabrouille et al. 2016). We calculated the total quasar luminosity and error from the 16th, 50th and 84th percentile of 1000 Monte Carlo integrations of the pure luminosity-evolution model of the Palanque-Delabrouille et al. (2016) quasar luminosity function.

We scale the peak of the eBOSS total quasar luminosity, which occurs at $z = 2.01$, to the Madau & Dickinson (2014) fitting function. From this, we determine the CSFH for spheroids by fitting an eight-point spline weighted by the inverse relative error squared using the compiled CSFH data for $z > 2.01$ and the eBOSS AGN data below this redshift (red line on Fig. 1). We elect to use the compiled CSFH data above the peak redshift because it is more comprehensive and precise than the AGN data – in the adopted model, about half of spheroid stellar mass forms prior to $z = 2.01$.

The eBOSS data represent optical luminosities, and thus do not capture activity from obscured AGN. Under the assumptions of the

model, an obscured fraction which evolves with redshift changes how quickly spheroid star formation activity declines since $z \sim 2$ if we maintain that the spheroid CSFH is equal to the total CSFH prior to that redshift. The evolution of the obscured AGN fraction as a function of redshift is still unclear. Treister & Urry (2006) find from quasar X-ray luminosity functions that the obscured fraction evolves as $(1 + z)^{0.3–0.4}$, while Lusso et al. (2013), also using X-ray data, find no evidence for evolution. The shape of the spheroid CSFH has direct consequences for the bulge to disc stellar mass ratio, and corresponding CSEDs, at $z = 0$. Adopting the evolution in Treister & Urry (2006) will result in a steeper drop-off in the spheroid CSFH, less spheroid stellar mass and a fainter spheroid CSED at $z = 0$. Conversely, adopting an X-ray luminosity density evolution that declines more slowly, as in, e.g. Ueda et al. (2014) results in the opposite. Similarly, adopting an earlier (later) peak will result in less (more) spheroid stellar mass and redder, fainter (bluer, brighter) emission at $z = 0$. Accurate bulge-disc decomposition over the $0.1 < z < 2$ range, and corresponding stellar mass estimates, will test these scenarios and allow the reconstruction of the disc and spheroid CSFHs without the need to adopt AGN activity as a proxy.

The CSFH for discs (solid blue curve in Fig. 1) is determined by fitting an eight point spline to the Madau & Dickinson (2014) CSFH data minus the CSFH for spheroids. Each spline is then extrapolated to cover lookback times between 0 and 13.5 Gyr. We also impose a CSFH floor of $10^{-4} \, M_{\odot} \, yr^{-1} \, Mpc^{-3}$ to reduce the numerical integration error arising when deriving the stellar mass density in spheroids.

The resulting CSFH functions and data are shown in Fig. 1. The transition from spheroid star formation to disc star formation happens ~ 1 Gyr later ($z \sim 1.2$ compared to $z \sim 1.7$) in this model compared to Driver et al. (2013). This is due to the use of the eBOSS AGN data, and a higher CSFH for spheroids at very high redshift because we fit to the CSFH data instead of the AGN data. Combined with using spline fitting to avoid assuming a functional form, this improves the fitting of the CSFH at high redshifts over the Driver et al. (2013) model. The precise shape of the disc CSFH at $t \sim 5$ Gyr is, to some degree, a byproduct of the spline fitting and subtraction and has little physical significance. Otherwise, the fitting functions are similar to those adopted by Driver et al. (2013) for the CSFH for spheroids and discs (dashed lines).

We estimate the error associated with the CSFH by repeating the spline fitting procedure for the lower and upper bounds of the individual CSFH data points and show the error regions on Fig. 1. The resulting ≈ 40 per cent error in the total CSFH at $z = 0$ represents a conservative estimate of the error in the CSFH by itself. It is more reasonable as an estimate of total model error, which incorporates uncertainties in the model assumptions, the IMF, stellar libraries and gas phase metallicity.

3.2 Model stellar populations

To model the stellar population, we use the GALAXEV software and the Bruzual & Charlot (2003) stellar models for consistency with the Andrews et al. (2017b) empirical CSED measurement. Both the Bruzual & Charlot (2003) and PEGASE 2 (Le Borgne et al. 2004) model used by Driver et al. (2013) employ the same set of Padova (1994) isochrones, but differ in their underlying library of stellar atmospheres – Bruzual & Charlot (2003) uses the theoretical BaSeL library (Allard & Hauschildt 1995) while PEGASE 2 uses the empirical ELODIE library (Prugniel & Soubiran 2001). The difference between the two stellar libraries should be small over the relevant wavelength range (Conroy & Gunn 2010). A detailed exploration of
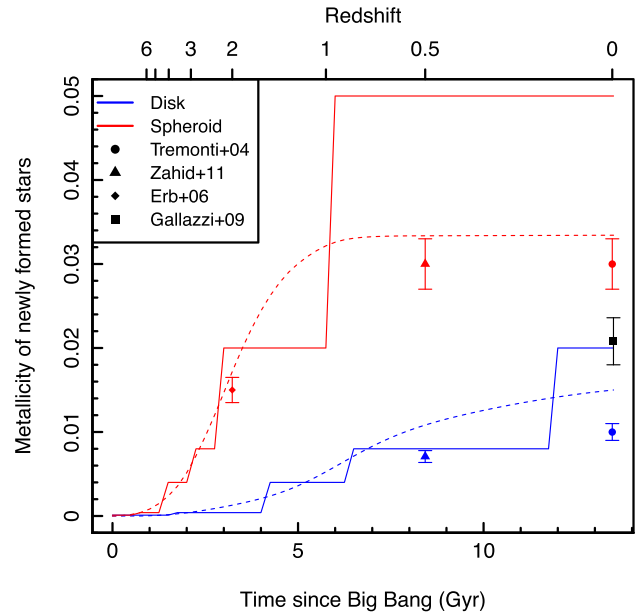

Figure 2. The adopted metallicity of newly formed stars for spheroids (red) and discs (blue). Metallicity curves in the absence of rounding are shown in dashed lines. The inferred metallicities of spheroids and discs, from Driver et al. (2013) based on the underlying Tremonti et al. (2004), Erb et al. (2006) and Zahid et al. (2011) data, as well as the cosmic stellar phase metallicity (Gallazzi et al. 2009) are also shown.

the effect of assuming different stellar libraries on the empirical and model CSEDs would require refitting SEDs to subsamples of the Driver et al. (2017) catalogue and is outside the scope of this paper. Regardless, any differences are not likely to be significant in light of measurement and other model uncertainties. If the BC03 libraries are found to be insufficiently accurate, the CSED measurements and models will need to be revised accordingly.

We use a Chabrier (2003) IMF, again to be consistent with the empirical CSED measurement. [The Driver et al. (2013) model uses a Baldry & Glazebrook (2003) IMF, which can be converted to a Chabrier IMF by scaling the CSFH appropriately.]

We compute model spectra in 0.25 Gyr time-steps using the adopted CSFH splines evaluated at 10 Myr intervals. We adopt a metallicity of newly formed stars that increases linearly with stellar mass formed for each component with no time lag (i.e. instantaneous enrichment), similar to Driver et al. (2013). However, unlike PEGASE 2 which has a broad range of metallicities, the Bruzual & Charlot (2003) models are only computed for six different discrete metallicities – $Z = 0.0001, 0.0004, 0.004, 0.008, 0.02 \, (Z_{\odot})$ and 0.05. We do not interpolate between metallicities which is considered bad practice, but round to the nearest available Bruzual & Charlot (2003) model (see Fig. 2). We also require the metallicity to reach $Z_{\odot}$ at $t = 3.25$ Gyr for spheroids and $0.75 \, Z_{\odot}$ at $t = 13.5$ Gyr for discs. This choice is guided by the Driver et al. (2013) model, which reaches metallicities of 0.01 and 0.03 for spheroids and discs respectively and the underlying Tremonti et al. (2004); Erb et al. (2006) and Zahid et al. (2011) data, but sets a higher metallicity for discs. The Driver et al. (2013) prescription reaches a cosmic stellar phase metallicity significantly lower than the $1.04 \pm 0.14 \, Z_{\odot}$ at the current epoch (Gallazzi et al. 2009), so we adopt a higher trajectory for the disc metallicity. The adopted metallicity evolution, with and without rounding, is shown in Fig. 2.
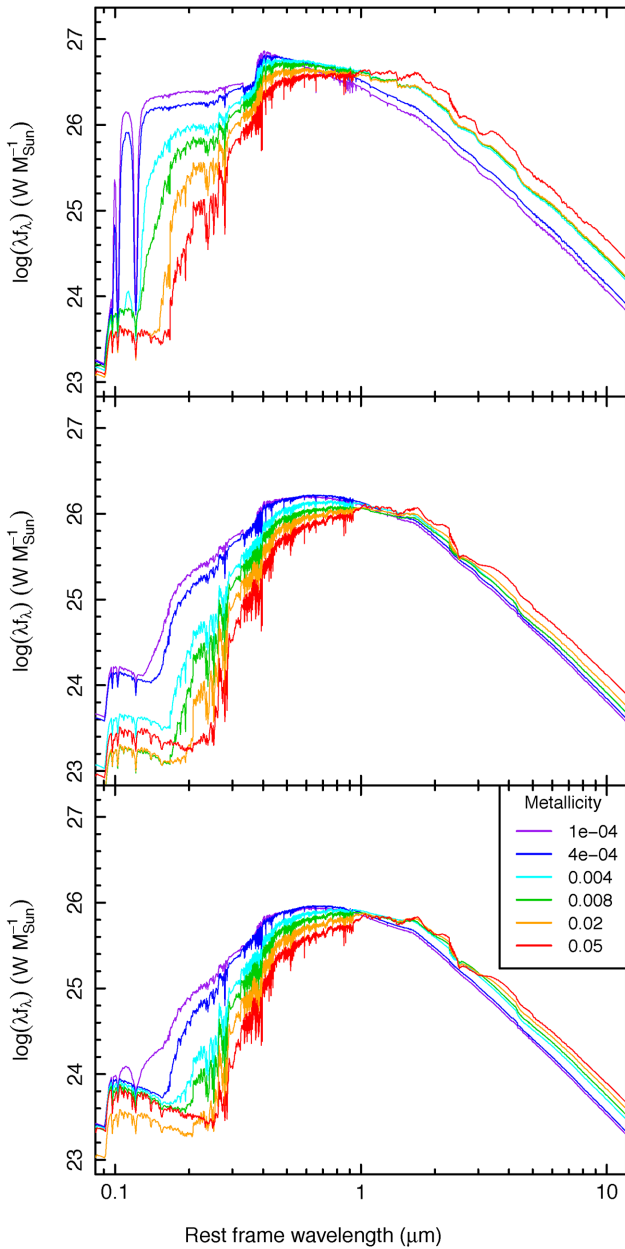
From our adopted CSFH, IMF and metallicity evolution, 61 and 74 per cent of stellar mass forms at metallicities between 0.004 and 0.02 for both spheroids and discs, where the near-infrared flux difference is negligible. Imprecision in modelling metallicities may affect the blue portion of the spheroid CSED notably, but the impact on the overall CSED is minimal.

3.3 Dust modelling

To model dust attenuation we use the Charlot & Fall (2000) extinction model built in to GALAXEV. We set the V-band optical depth (τ_V) as seen by stars in birth clouds to

$$\tau_V(t)^a = X \exp\left(\frac{-t}{2.5}\right) \int_0^t 0.004 \, \text{csfh}(t') \exp\left(\frac{t'}{2.5}\right) \mathrm{d}t', \qquad (1)$$

where t and t' are ages of the Universe in Gyr, X is the normalization constant necessary to yield $\tau_V(13.5 \, \text{Gyr}) = 1.2$ for discs and 0.25 for spheroids, csfh(t) is the CSFH for spheroids or discs and $a = 2$ for discs and 1/0.65 for spheroids. The right-hand side of the τ_V model is the dust mass density evolution from Driver et al. (2017). This model is based on measurements of the dust mass density by Ménard & Fukugita (2012) and Béthermin et al. (2014), and predicts that 0.4 per cent of mass forming into stars returns to the ISM as dust, with an exponential destruction with a characteristic time of 2.5 Gyr (see Driver et al. 2017 for details). We choose the model involving exponential dust destruction – the alternative model where some fraction of dust survives indefinitely is inconsistent with elliptical galaxies being largely dust free at $z = 0$. The values of $\tau_V(13.5 \, \text{Gyr})$ are chosen to yield a time evolution consistent with the median $\tau_V(13.5 \, \text{Gyr})$ value from the Driver et al. (2017) fits. We apply a similar prescription to the fraction of attenuation arising in the ISM μ, setting $\mu(13.5 \, \text{Gyr})$ to be 20 and 4 per cent for discs and spheroids, respectively. The chosen values for μ are guided by the median $\mu(z < 0.06)$ derived from spheroid and disc samples created by matching against the GAMA VisualMorphologyv03 catalogue[1] Ultimately, the values of $\tau_V(13.5 \, \text{Gyr})$, $\mu(13.5 \, \text{Gyr})$ and the free parameter a for discs are chosen to reproduce the ultraviolet, post-attenuation CSED for $0 < z < 1$ (especially at lower redshifts). The corresponding values regarding spheroids are less certain, but are chosen such that the resulting ultraviolet extinction is consistent with the empirical data. These functions and estimates are shown in Fig. 4. The error bars shown represent the 16th and 84th percentile of the distribution as an indication only; we acknowledge that our empirically derived dust attenuation parameters are subject to large SED modelling errors due to limited sensitivity in the far-infrared at the current time.

We model the far-infrared emission with models from Dale et al. (2014) scaled up to the total energy attenuated. Dale et al. (2014) model the emission from dust exposed to 64 different heating intensities as described by the parameter α_{sf}, where model 1 ($\alpha_{sf} = 0.0625$) has the most heating and model 64 ($\alpha_{sf} = 4.0000$) the least. These models improve on the Dale & Helou (2002) models used by Driver et al. (2013) by updating the mid-infrared observations on which the models are based and adding in emission from the dust torii of AGN. The main difference between these models and those used by MAGPHYS in the Andrews et al. (2017b) empirical

Figure 3. Unattenuated SEDs for simple stellar populations constructed using the CSFH for discs 8 Gyr after the big bang with the indicated metallicities at an age of 1 Gyr (top), 5 Gyr (centre) and 10 Gyr (bottom). The units on the Y-axis are watts per solar mass of stars formed.

For illustration purposes, Fig. 3 shows SEDs for simple stellar populations with ages 1, 5 and 10 Gyr as a function of metallicity. The input CSFH is that for discs at 8 Gyr after the big bang. While the model CSEDs vary considerably in the ultraviolet and short-wavelength optical, the total flux output varies by only 0.3 dex in the near-infrared between the most extreme metallicities. The least scatter occurs in the rest-frame Y band – at 1 μm, flux ranges from $10^{26.44}$ W per solar mass of stars formed ($Z = 0.0001$) to $10^{26.64}$ W M$_\odot^{-1}$ ($Z = 0.004$) at $t = 1$ Gyr. The spread decreases to between $10^{26.07}$ W M$_\odot^{-1}$ ($Z = 0.0004$) to $10^{26.14}$ W M$_\odot^{-1}$ ($Z = 0.008$) at $t = 5$ Gyr and $10^{25.82}$ W M$_\odot^{-1}$ ($Z = 0.004$) to $10^{25.91}$ W M$_\odot^{-1}$ ($Z = 0.05$) at $t = 10$ Gyr.

---

[1] The spheroid value was derived from an elliptical sample defined by P_EL_DEBIASED > 0.7, while the disc value was derived from a subsample of Sd-Irr galaxies (HUBBLE_TYPE_CODE = 15). The corresponding values of τ_V for these samples are implausible.
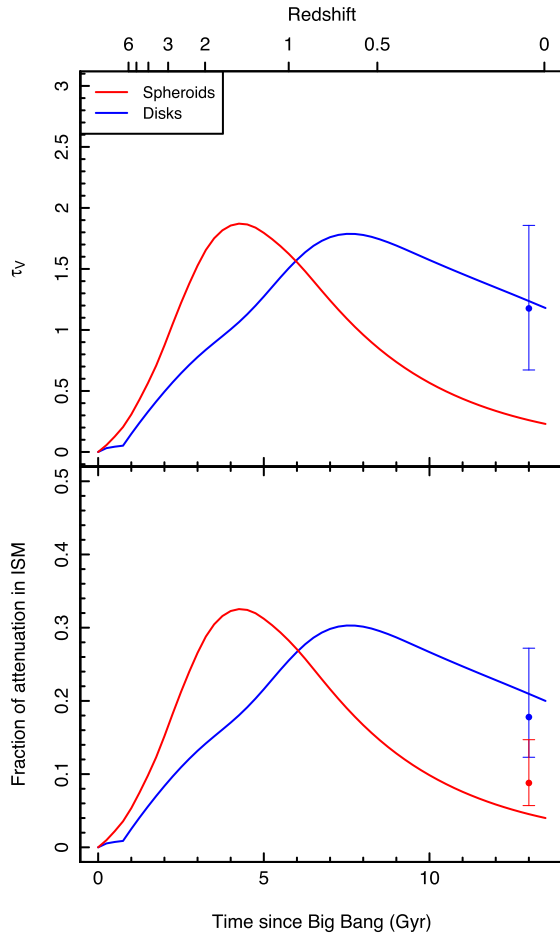
Figure 4. The adopted τ_V (top) and μ (bottom) for spheroids (red) and discs (blue).

the combination of which reproduces the Andrews et al. (2017b) far-infrared CSED between 100 and 500 µm for $z < 0.14$ well. At higher redshifts, we evolve the luminous galaxy model selection by selecting $\alpha_{sf} = 1.3750 + 0.6875 \log(\text{CSFH}(13.5 \text{ Gyr}))/\log(\text{CSFH}(t))$, with α_{sf} for normal galaxies being 0.500 greater than that for infrared luminous galaxies. This evolves the dust emission spectra towards a higher temperature on average – from 25–32 K at $z = 0$ to 32–41 K at the peak of star formation at $z \sim 2$ – in accordance with increased far-infrared emission and the L_{ir}–T_{dust} relation (Symeonidis et al. 2013). These dust temperatures are also consistent with those observed by Symeonidis et al. (2013) over this redshift range. A weak dependence on the CSFH is also expected as increased heating from a higher CSFH is partially offset by increased dust masses, as noted by Symeonidis et al. (2013) and Driver et al. (2017). This particular selection appears to reproduce the Andrews et al. (2017b) far-infared CSED well, however we caution that this estimate is based on a significant fraction of extrapolated flux. Furthermore, the Symeonidis et al. (2013) data probe galaxies with $L_{ir} > 10^{10} \, L_{\odot}$ increasing to $10^{11.8} \, L_{\odot}$ at $z = 1$, and the normal infrared galaxy population out to $z = 0.3$, representing an incomplete picture of dust temperatures across the galaxy population out to $z = 1$.

3.4 AGN modelling

We represent emission from AGN in two classes – obscured and unobscured. We derive an unobscured AGN composite spectrum from the sum of the SDSS composite quasar spectrum published by vanden Berk et al. (2001) and the 100 per cent AGN fraction Dale et al. (2014) model. To obtained an obscured AGN spectrum, we multiply the quasar composite spectrum by the IPEF as measured by Andrews et al. (2017b) for $0.82 < z < 0.99$ to represent dust attenuation and add the hottest Dale et al. (2014) model (number 1) to represent attenuation of AGN emission in the broader ISM. We scale the obscured and unobscured AGN spectra to yield a g-band rest-frame luminosity equal to 2 and 1 times the eBOSS integrated g-band luminosity of Palanque-Delabrouille et al. (2016) respectively (the Palanque-Delabrouille et al. 2016 data trace the evolution of unobscured AGN) for an obscured to total AGN emission ratio of 67 per cent. Observations indicate a ratio of obscured to total AGN emission ranging between 41 and 77 per cent, with the majority of estimates towards the upper end (Richards et al. 2006; Buchner et al. 2015). This ignores the evolutionary biases traced by AGN (e.g. being more common in dust-free early-type galaxies), but the impact of this assumption should be limited by the high photon escape fractions for these systems. AGN host galaxies were not included in the Driver et al. (2017) fits, and do not represent a significant addition to the Andrews et al. (2017b) CSED at any $z < 0.99$ – Andrews et al. (2017b) find an extra 5–10 per cent contribution to the CSED from X-ray emitting AGN and their host galaxies except possibly in the ultraviolet as noted by Driver et al. (2016c).

4 MODEL OUTPUTS

4.1 The unattenuated CSED

Fig. 5 shows the predicted unattenuated CSED ϵ_{int} (rest frame, in λf_λ units) from our phenomological model (black: total, blue: disc, red: spheroid) with shaded areas representing model uncertainty compared to the unattenuated Andrews et al. (2017b) estimates (for $0.02 < z < 0.99$) at the relevant time-steps (green band and line).
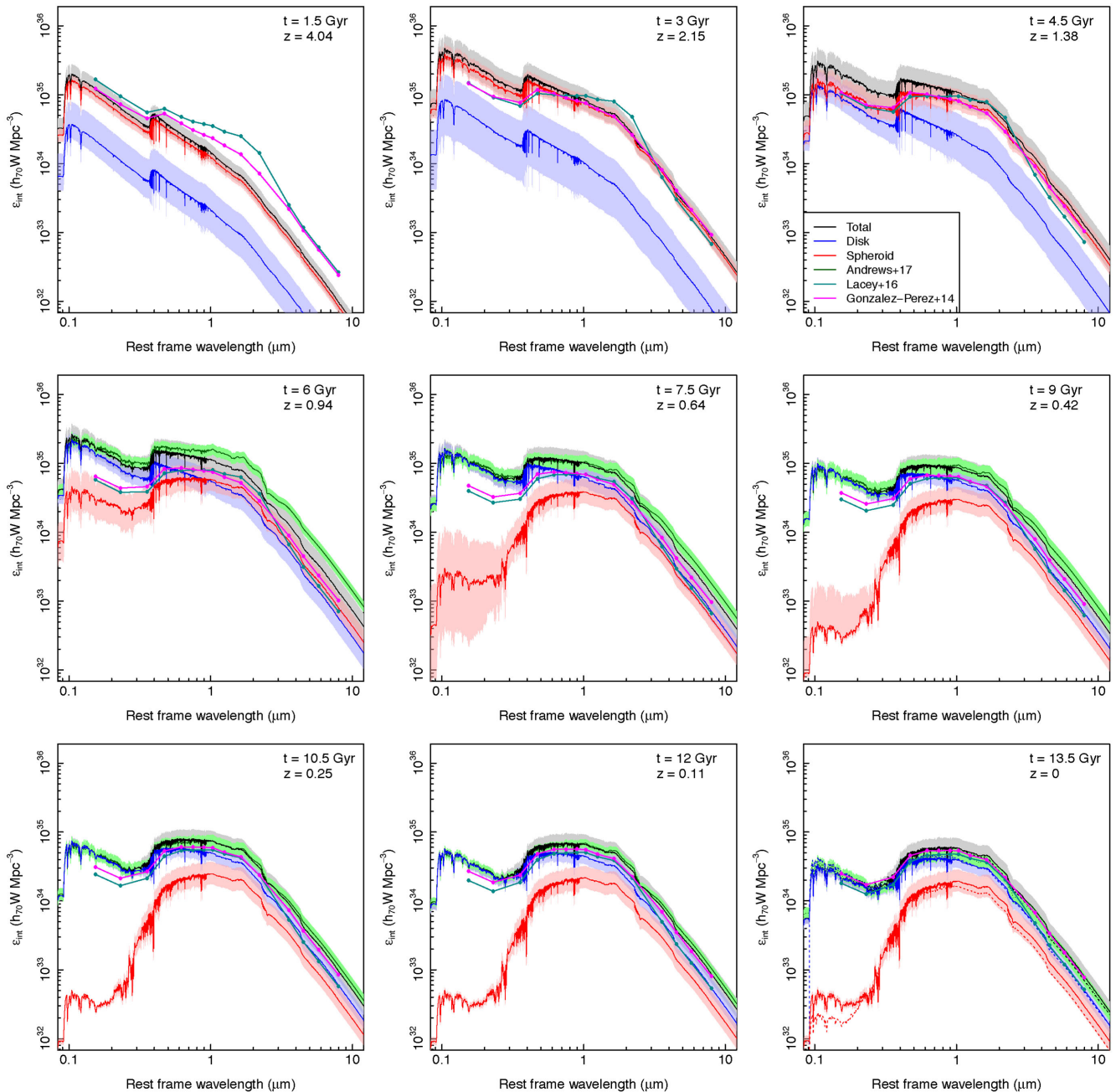
CSED estimates is that the Dale et al. (2014) models produce less 70 µm emission. This difference is immaterial given the lack of constraining data near this wavelength. As the Dale et al. (2014) templates are in arbitrary units, we scale to reflect the total attenuated energy implied by our stellar model and equation (1) (integrated over 10 nm $< \lambda < 8$ µm).

Initially we select the set of models with a zero AGN fraction. At all redshifts, we assume 15 per cent of the far-infrared radiation emitted originates from galaxies with warmer dust temperatures (such as ultra-luminous infrared galaxies) and 85 per cent from the broader infrared galaxy population. This assumption is reasonable, given >90 per cent of the normal infrared galaxy population and >60 per cent of the luminous infrared galaxy population have dust temperatures <35 K out to $z = 0.5$ (Symeonidis et al. 2013). This ratio is slightly lower than the 25 per cent contribution from ultra-luminous infrared galaxies to the IGL at 140 µm modelled by Chary & Elbaz (2001), however we find the lower ratio represents a better fit to the Andrews et al. (2017b) attenuated CSEDs. This is not definitive, given that the photometry underlying the Andrews et al. (2017b) far-infrared CSEDs is of relatively low depth and sensitivity; this also prevents computation of robust total infrared luminosity functions.

We select model 33 ($\alpha_{sf} = 2.0625$) and 37 ($\alpha_{sf} = 2.3125$) for infrared luminous and normal galaxy populations respectively at $z = 0$,

Figure 5. The model unattenuated CSED for spheroids (red), discs (blue) and both combined (black), with shaded areas representing model uncertainty. The Andrews et al. (2017b) data are also given (green line/band), with the uncertainty range indicating the error in the normalization of the CSED only. We also extrapolate this data to $z = 0$. Semi-analytic predictions from GALFORM are shown in dark cyan (Lacey et al. 2016) and pink (Gonzalez-Perez et al. 2014). An animated version of this figure is available online as supporting information.

While not shown in the figure (as the data probe a period between 12.2 and 13.3 Gyr), the Driver et al. (2012) model lies within, but close to the lower bound of the uncertainty range of the CSED measurement. We also extrapolate the Andrews et al. (2017b) CSED estimates to $z = 0$ by rescaling the $0.02 < z < 0.08$ CSED by the expected decline in total integrated energy. The error range depicted in Fig. 5 for the Andrews et al. (2017b) data represents the error in the normalization of the CSED only and does not incorporate any contribution from errors in SED modelling, incompleteness or photometry.

From Fig. 5, we can extract a number of key conclusions. The changeover from major mergers (spheroid formation) to cold gas accretion (disc formation) – where emission from discs dominates in the rest-frame ultraviolet – occurs at $z \sim 1.2$, in line with the CSFH (see Fig. 1). Cold gas accretion primarily occurs in low-mass ($M_* < \sim 5 \times 10^{10}\,\mathrm{M}_\odot$ for a $0 < z < 0.5$ GAMA sample) galaxies, with merger accretion continuing in high-mass galaxies (Robotham et al. 2014). The total energy output of the Universe reaches a maximum of $5.0^{+2.7}_{-1.6} \times 10^{35}\,h_{70}$ W Mpc^{-3} at $z \approx 2.1$, while energy output from discs reaches a maximum of just $2.7^{+1.0}_{-0.7} \times 10^{35}\,h_{70}$

W Mpc^{-3} at $z \approx 0.8$. To date, just above half (50.6 per cent) of the energy generated by the Universe was generated by objects now residing in discs, with the other half being generated by material now residing in spheroids. For reference, 50 per cent of the stellar mass today resides in spheroids, with the other 50 per cent in discs (Moffett et al. 2016b).

Recall that the model is calibrated on the CSFH, and therefore is designed to reproduce the (unattenuated) ultraviolet emission. However, the Andrews et al. (2017b) empirical CSEDs have a number of caveats which may become reflected in the model. First, the empirical CSEDs may suffer from incompleteness due to Malmquist bias, resulting in the omission of low-mass, blue, star-forming systems. Andrews et al. (2017b) estimate that this incompleteness causes of the order of 20 per cent of the ultraviolet flux to be missed. Secondly, the Wright et al. (2016a) catalogue, on which the empirical CSEDs are based, measures ultraviolet flux in an optically defined aperture convolved with the *GALEX* point spread function. This approach may miss additional, extended ultraviolet emission from disc galaxies (Gil de Paz et al. 2005; Thilker et al. 2007) for $z < 0.45$.

Our model reproduces the unattenuated CSED in the near-infrared well, except arguably at $z \sim 0.9$, where we see a slight deficit in the model. Uncertainties in the near-infrared may be the result of a number of factors:

(i) Uncertainties in modelling thermally pulsating asymptotic giant branch stars. We have tried to control for this effect, as both the phenomological model and CSED estimates are based on the Bruzual & Charlot (2003) stellar libraries.

(ii) Uncertainties and imprecisions in modelling gas-phase metallicity. However, Fig. 3 shows these have a much greater effect in the ultraviolet and optical shortward of the 4000 Å break and opposite effects either side of about 1 μm. This would suggest that the lack of metallicity interpolation is not the dominant source of modelling error.

(iii) The photometric and spectroscopic data underlying the Andrews et al. (2017b) measurements use an observed frame *r*- or *i*$^+$-band selection. At the high-redshift ends of GAMA and G10/COSMOS, this is equivalent to *u* or *g* in the rest frame. It is, hence, likely that some quiescent or very dusty galaxies are excluded.

(iv) The Driver et al. (2013) model applies a 25 per cent downward adjustment to the CSFH for spheroids, resulting in a spheroid to disc mass ratio at the current epoch of $\sim \frac{2}{3}$. This renormalization is not necessary in our model – see Section 6.4.

Overall, our phenomological model appears to reproduce the Andrews et al. (2017b) unattenuated CSED for $z < 1$ extremely well. The black model line lies close to, or within the green measurement band (which takes into account uncertainty in the normalization of the CSED only, excluding the biases noted above and in Andrews et al. 2017b) at all redshifts – with just a minor discrepancy in the near-infrared CSED in the $0.82 < z < 0.99$ bin. The model uncertainty at optical wavelengths and low redshifts is mostly due to uncertainty in the CSFH at high redshifts. An animated version of Fig. 5 is available online as supporting information.

4.2 The attenuated CSED

We now add in our dust prescription as described in Section 3.3 to determine the attenuated (as observed) CSEDs. Fig. 6 shows the resulting attenuated CSED ϵ_{obs}, now with far-infrared emission at various time-steps with the Andrews et al. (2017b) attenuated CSED data at the relevant time-steps. The Andrews et al. (2017b) data have

been extrapolated to $z = 0$. The Driver et al. (2012) model, being relevant for $0.013 < z < 0.1$ and thus not shown above, generally lies within the uncertainty range of the empirical CSED estimates. Again, the error range in the empirical CSEDs reflects the error in the normalization of the CSED only, excluding uncertainties in SED modelling and the underlying photometry.

Both optical and far-infrared emission reach a maximum of $2.2^{+1.4}_{-0.8}$ and $3.7^{1.7}_{-1.1} \times 10^{35} h_{70}$ W Mpc^{-3} at $z \approx 2.1$.

The most noticeable disagreement between the phenomological model and the CSED data occurs at around 70 μm. Empirically, MAGPHYS is unable to constrain the warm dust peak resulting from the lack of sufficiently deep 70 μm data in both the GAMA and G10/COSMOS data sets. The choice of different dust emission templates to model the far-infrared emission is also important – Driver et al. (2012) use the average of Dale & Helou (2002) models 34 and 40, which results in a small warm dust peak that is slightly below our model curve. Ultimately, the far-infrared imaging data underlying the SED fits is of poorer quality in terms of resolution and sensitivity – the CSED estimates are only precise to a factor of about 2 at low redshifts, increasing to a factor of 5 beyond $z = 0.45$. Estimates in G10/COSMOS are based on a significant fraction of extrapolated flux, while in GAMA the low detection rate undermines the reliability of the corresponding CSED (see fig. 7 in Andrews et al. 2017b). We denote wavelength intervals where the CSED estimates may be unreliable with a dashed (as opposed to solid) line. For this reason, a rigorous optimization against the Andrews et al. (2017b) CSED estimates between 100 and 500 μm is not possible.

Otherwise, our phenomological model again reproduces the attenuated CSED well at all redshifts – lying within or close to the green error bounds of the normalization of the CSED only (which excludes SED modelling error, incompleteness and bias) with two exceptions, the first being the $z \sim 0.91$ shortfall in the near-infrared mentioned previously. Secondly, the model overpredicts flux at 20 μm. This is a consequence of differing prescriptions of warm dust used by the empirical CSED measurements and the model predictions, coupled with the difficulty of correctly modelling emission from polycyclic aromatic hydrocarbons and the incompleteness of the observational data at this wavelength. An animated version of Fig. 6 is available online as supporting information.

5 SEMI-ANALYTIC MODELLING WITH GALFORM

The phenomological model described in Section 3 is a simplistic description built explicitly to model the CSED, providing an instant CSED prediction at any redshift to help interpret the EBL and photon escape fraction (see below). While it has predictive power outside this domain – one can infer the cosmic stellar and dust mass densities – many phenomena are neglected (for example, variations with environment). Semi-analytic models are able to provide a broader understanding, but at the expense of additional complexity.

Here, we use two recent versions of the GALFORM semi-analytic model (Gonzalez-Perez et al. 2014; Lacey et al. 2016) to derive predictions of the CSED across cosmic time. We derive predictions for the CSED for snapshots close to the mean redshift in the Andrews et al. (2017b) redshift bins and at $z = 1.173$, 1.504, 2.070, 2.422, 3.060, 3.576, 4.179, 4.520, 5.724 and 6.197. For each snapshot, we compute the pre- and post-attenuated rest-frame luminosity distributions as they would be observed through *GALEX*, SDSS, UK Infrared Telescope, IRAC bands and at 24, 60, 100, 160,
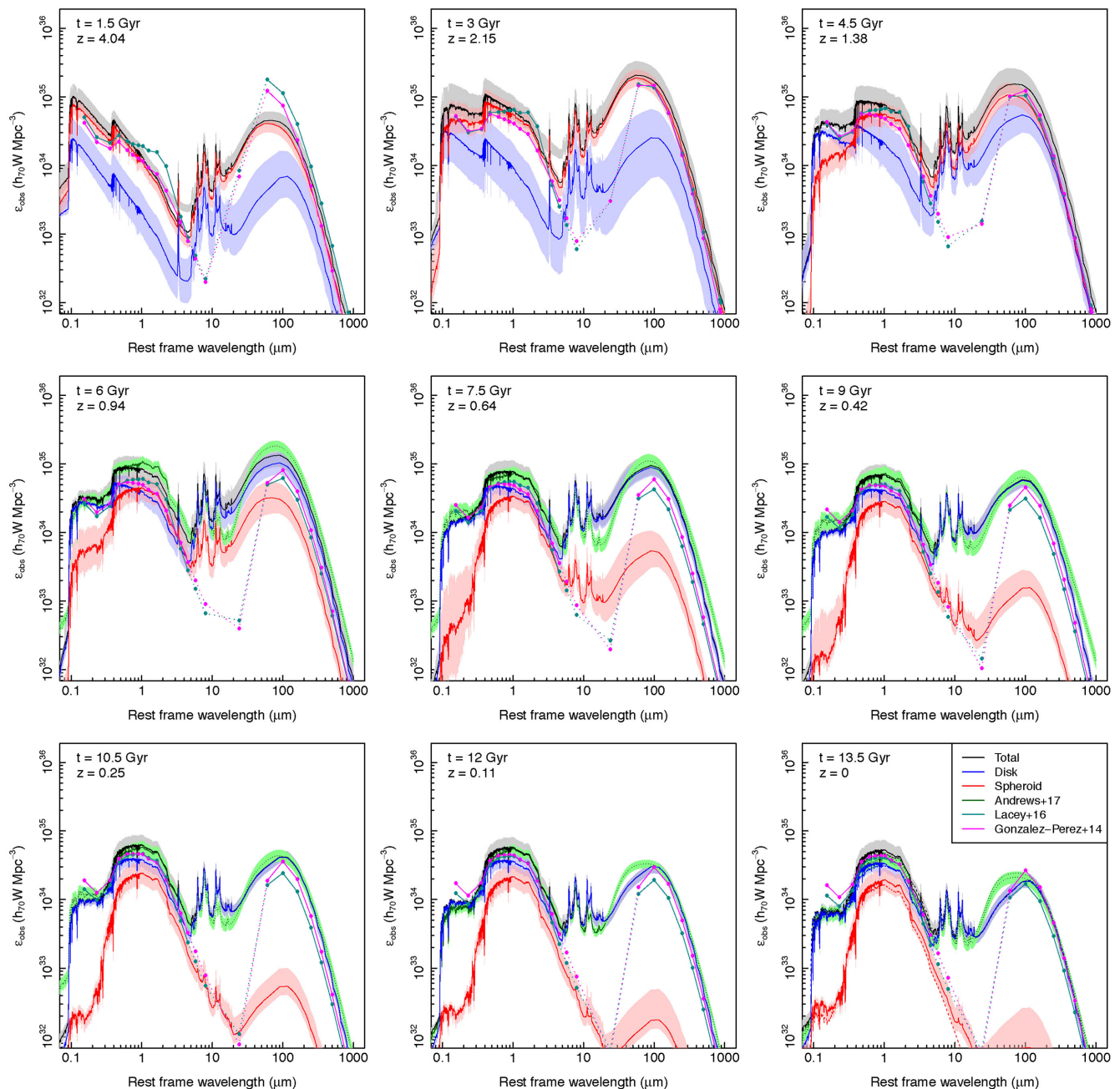
Figure 6. The model attenuated CSED with labelling equivalent to Fig. 5. Wavelength intervals where the Andrews et al. (2017b) CSEDs may be deemed less reliable due to the lack of underlying photometric data and where semi-analytic predictions from GALFORM omit flux from warm dust are denoted with a dotted line. An animated version of this figure is available online as supporting information.

250, 350, 500, 850 and 870 μm. We then multiply by the respective luminosities and sum to arrive at the corresponding luminosity density for each band. The resulting predicted (rest frame) unattenuated and attenuated CSEDs are shown in Figs 5 and 6, respectively – the Lacey et al. (2016) is denoted with dark cyan curves, while the Gonzalez-Perez et al. (2014) model is denoted with pink curves.

The two GALFORM flavours presented here were calibrated to fit the B_j- and K-band luminosity functions at $z = 0$, and the evolution of the K-band luminosity function out to $z \sim 3$. In addition, the Lacey et al. (2016) model paid close attention to number counts and redshift distributions of sources observed by *Herschel* and at

850 μm. Therefore, the comparisons we derive here (i.e. the IGL and evolution of the CSED) are mostly independent tests that can offer valuable insight into how the models can be improved.

These instances of GALFORM split star formation into two modes in a similar manner as our phenomological model – a quiescent mode, driven by cold gas accretion on to discs and a starburst mode, where galaxy mergers and disc instabilities transfer disc gas into spheroids triggering a starburst. The primary difference between the two versions of GALFORM is the choice of IMF. The Lacey et al. (2016) version employs different IMFs for spheroids and discs – Kennicutt (1983) for disc star formation and a custom, top-heavy IMF – a power law with a tunable slope between 0 and 1

– for spheroid star formation. In contrast, the Gonzalez-Perez et al. (2014) version assumes a Universal Kennicutt (1983) IMF. GALFORM predicts an earlier transition from spheroid to disc formation than the phenomological model – $z \sim 3$ compared to $z \sim 1.2$ (see Lacey et al. 2016, fig. 26).

Mock photometry is computed in the Lacey et al. (2016) model using the Maraston (2005) stellar population synthesis codes, while the Gonzalez-Perez et al. (2014) model uses the Bruzual & Charlot (2003) libraries. The Maraston (2005) libraries track fuel consumption, in contrast to the isochrone analysis employed by Bruzual & Charlot. The modelling of thermally pulsating asymptotic giant branch stars is still controversial, with the Maraston libraries arguably overestimating the near-infrared emission (see e.g. Maraston 2005; Maraston et al. 2006; Bruzual 2007; Conroy & Gunn 2010; Bruzual et al. 2013; Noël et al. 2013; Capozzi et al. 2016). The use of the Maraston stellar libraries is the most likely cause of the near-infrared enhancement of the Lacey et al. (2016) model over both the phenomological model and the Gonzalez-Perez et al. (2014) model at $z > 1$ in both the unattenuated and attenuated CSEDs (see Figs 5 and 6).

GALFORM can also compute dust attenuation via radiative transfer through a two-phase medium consisting of molecular clouds and the diffuse ISM, with dust emission described using a modified blackbody spectrum (Lacey et al. 2016). GALFORM does not model the mid-infrared emission as it does not incorporate polycyclic aromatic hydrocarbons (Cowley et al. 2017). As a consequence, the predicted attenuated CSED is unreliable between 8 and 70 µm rest frame. This region is denoted with a dotted line in Fig. 6.

Both GALFORM models underpredict the CSFH for $z < 3$ (Mitchell et al. 2014; Guo et al. 2016; Lacey et al. 2016) compared to literature estimates (e.g. Madau & Dickinson 2014). The predictions, however, agree with the lower CSFH derived by Driver et al. (2017) (on which the empirical CSED estimates are based). However, GALFORM produces a fainter unattenuated CSED than our empirical results. When adjusted for this offset, both semi-analytic models produce a shape of the unattenuated CSED that is very similar to our CSED estimates. Beyond $z = 3$, the GALFORM predictions of the CSFH show a better agreement with observations. Far-infrared emission grows faster than optical emission in both iterations of GALFORM at very high redshifts. This originates from obscured star formation in ultra-luminous infrared galaxies, which contribute a much greater portion of the total far-infrared luminosity at higher redshifts (Lagos et al. 2014). This effect is not accounted for in the phenomological model.

When adjusted for the offset in the CSED normalization, both GALFORM models reproduce the shape of the optical and near-infrared attenuated CSED well out to $z = 1$ (Fig. 6). Naïvely, the Gonzalez-Perez et al. (2014) model yields a better fit in the far-infrared. However, when adjusted, both models overpredict the ultraviolet CSED, with the Lacey et al. (2016) model being closer to the empirical data. We suspect the underpredicted dust attenuation is a result of overpredicted galaxy sizes – Merson et al. (2016) show that GALFORM is able to derive reasonable predictions for dust attenuation when the predicted half-mass radii are also plausible. However, galaxies with overpredicted sizes have much less attenuation than expected, as the diffuse dust component has a lower surface density.

In summary, both iterations of GALFORM underpredict the CSFH for $z < 3$ and thus the normalization of the unattenuated and attenuated CSEDs. Both semi-analytic models are able to reproduce the shape of the unattenuated and attenuated CSEDs well out to $z < 1$, with the exception that both models seem to underpredict the ultraviolet attenuation over $0 < z < 1$. In the absence of higher redshift CSED estimates, we look to constraints on the EBL, COB and CIB.

6 APPLICATION OF THE MODEL

Having developed a model which replicates the unattenuated and attenuated CSEDs for $z < 1$, we can now explore predictions of related quantities, such as the photon escape fraction, IGL, and stellar and dust mass densities compared to observations.

6.1 The integrated photon escape fraction

The IPEF represents the attenuated CSED divided by the unattenuated CSED. It is a simplistic but useful representation of the effects of dust attenuation. It is particularly useful for correcting ionizing radiation pervading the ISM and/or determining unattenuated star formation rates. The predominant source of error in the IPEF arises from SED modelling and incompleteness – the uncertain normalization due to cosmic variance, sampling and the use of photometric redshifts is divided out. The uncertainty arising from the CSFH also cancels.

Fig. 7 shows IPEFs as a function of redshift for both our model (smoothed with a spline interpolation) and the Andrews et al. (2017b) data (green shaded band). The disc IPEF reproduces the Andrews et al. (2017b) IPEFs well, especially at lower redshifts. The overall IPEF reaches a minimum longwards of $\lambda = 700$ nm at $z \sim 1.7$. The ultraviolet IPEF has two minima – one at $z \approx 1.7$, the other at $z \approx 0.6$. Spheroids become more transparent than discs across the electromagnetic spectrum at $z \sim 0.9$. Our methodology assumes dust emission is negligible. The spike in the photon escape fraction at approximately 3 µm is a consequence of the 3.3 µm polycyclic aromatic hydrocarbon emission feature and should not be regarded as an estimate of the photon escape fraction at that wavelength.

As noted before and in Gonzalez-Perez et al. (2017), both iterations of GALFORM underpredict the amount of dust attenuation for $z < 1$ compared to the Andrews et al. (2017b) empirical CSED estimates. The lack of a prescription for warm dust is the most likely cause for the shortfall in the mid-infrared.

One commonly used method to measure the CSFH involves determining the rest-frame far-ultraviolet luminosity function and correcting it for attenuation (see e.g. Kennicutt 1998; Madau & Dickinson 2014), usually using either the Calzetti et al. (2000) law or the IRX ($=L_{ir}/L_{FUV}$)–β relation (Meurer, Heckman & Calzetti 1999). For the latter, A_{FUV} can be computed directly from IRX. Here, we simply compute A_{FUV} by convolving the IPEF with the *GALEX* FUV filter curve and converting to magnitudes. Fig. 8 shows predictions of A_{FUV} compared to the empirical data from Cucciati et al. (2012), Burgarella et al. (2013) and Andrews et al. (2017b). The phenomological model obtains predictions of A_{FUV} that are broadly consistent with the empirical data at most redshifts, while GALFORM generally underpredicts A_{FUV}. At $z \sim 4$, the phenomological model appears to predict a lower A_{FUV} than the literature. However, at these redshifts, dust attenuation starts to deviate from the IRX–β relation (Capak et al. 2015). These redshifts are beyond the scope of this paper.

6.2 The integrated galactic light

We now look to compare the predicted IGL from our model, as well as from the semi-analytic models to the recent IGL analysis of Driver et al. (2013). We also compare against the
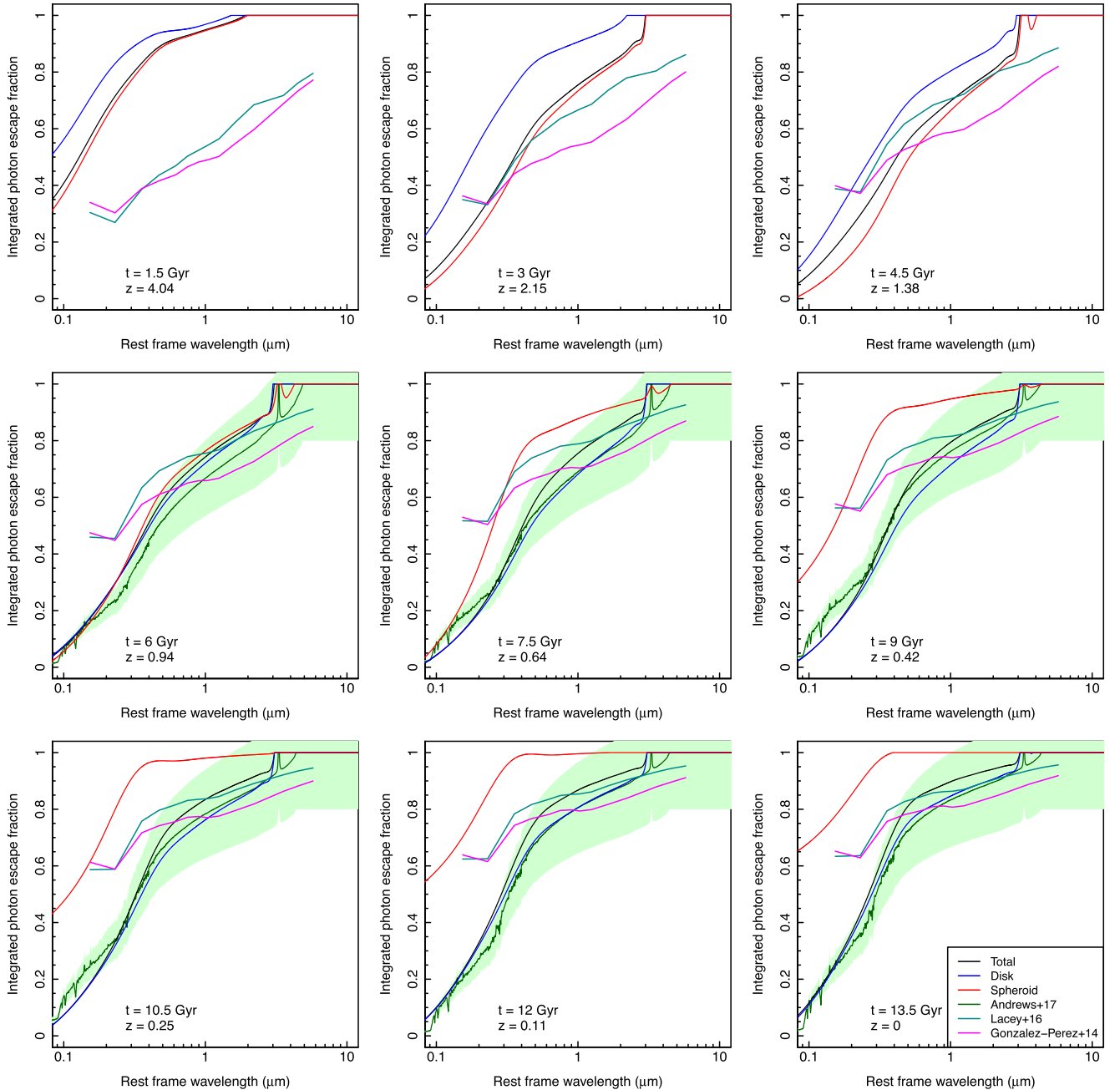
Figure 7. The model IPEF for spheroids (red), discs (blue) and both combined (black) with semi-analytic predictions from GALFORM (dark cyan, pink). The Andrews et al. (2017b) data are also given in green.

Gilmore et al. (2012) predictions from the semi-analytic model of Somerville et al. (2008) and Somerville et al. (2012). In short, this model uses a Chabrier (2003) IMF, the Bruzual & Charlot (2003) stellar libraries, a modified Charlot & Fall (2000) dust attenuation model and far-infrared spectra from Rieke et al. (2009), which are derived from (ultra)-luminous infrared and low-redshift galaxies.

The comoving EBL at redshift z is the amount of radiation received by an observer at a given epoch and may be derived from the (total) CSED as follows:

$$\text{EBL}(\lambda_{\text{obs}}, z) = \sum_{z'=z}^{z'=\infty} \frac{\epsilon(\lambda(1+z'), z')\mathrm{d}V(z')}{4\pi \, d_{\text{l}}(z')^2}, \qquad (2)$$

where $\epsilon(\lambda, z)$ is the rest-frame attenuated CSED at the redshift z, $d_{\text{l}}(z')$ is the luminosity distance at z to the volume corresponding to the redshift z' and $\mathrm{d}V(z')$ is the differential comoving volume of each model time-step subtending a solid angle of 1 sr.

Fig. 9 shows a comparison of our phenomenological model from Section 3 to measurements of the IGL at $z = 0$ (Driver et al. 2016c). Note that the phenomenological model curves are bumpy at wavelengths corresponding to the redshifted Lyman break and emission from polycyclic aromatic hydrocarbons due to the EBL summation involving discrete time-steps. The light blue shaded region denotes constraints on the EBL from the H.E.S.S. (H.E.S.S. Collaboration 2013) TeV gamma-ray observatory. These
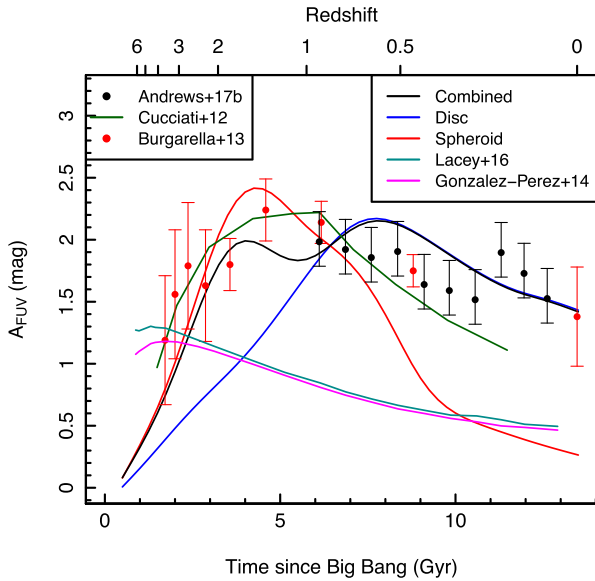
Figure 8. Rest-frame A_{FUV} as a function of redshift from the phenomological model (blue: disc, red: spheroids, black: weighted average by the cosmic star formation rate in each component), GALFORM, the Andrews et al. (2017b) estimates, Cucciati et al. (2012) and Burgarella et al. (2013).

observations are able to constrain the amplitude of the COB, but draw upon the Franceschini, Rodighiero & Vaccari (2008) and Domínguez et al. (2011) models, respectively, to define the shape. The red points represent γ-ray observations from Biteau & Williams (2015), which do not assume an EBL model spectrum.

As expected, emission from low-redshift discs dominates at ultraviolet, optical and far-infrared wavelengths. Longwards of 350 µm, we find that high-redshift spheroids represent the dominating contribution to the far-infrared IGL. In the near-infrared, spheroids at low and high redshift are the dominating contribution to the IGL. AGN make a small, but noticeable contribution of 0.34 nW m^{-2} sr^{-1} in the u band, and 0.7 nW m^{-2} sr^{-1} at 100 µm.

The phenomenological model is consistent with the Driver et al. (2016c) IGL measurements and the Gilmore et al. (2012) semianalytic model except in the ultraviolet. The phenomenological model becomes consistent with H.E.S.S. Collaboration (2013) at $\lambda > 300$ nm, suggesting an origin at low to intermediate redshifts.

However, there exists some scope for an upward adjustment in the (unobscured) AGN contribution to the EBL, given the Palanque-Delabrouille et al. (2016) measurements of the quasar luminosity density stop at $z = 0.68$ and are associated with an uncertainty of a factor of 2 at these redshifts. Another potential upward adjustment arises from low-level AGN activity at low and intermediate redshifts. The phenomenological model links high-level AGN activity to star formation, resulting in the steep drop off with redshift (see Fig. 1). The AGN radio luminosity density for low-luminosity ($L < 10^{25}$ W Hz^{-1}) sources declines relatively slowly with redshift – $L \propto (1 + z)^{1-2.5}$ (Smolčić et al. 2009; McAlpine, Jarvis & Bonfield 2013; Padovani et al. 2015) – a rate slower than, or similar to the decline in the total CSFH. For illustrative purposes, adding a low-power unobscured AGN component with a g-band luminosity of $\sim 9 \times 10^{32}$ W Mpc^{-3} at $z = 0$ (i.e. ~ 3 per cent of the convolved, attenuated CSED in g at $z = 0.05$) evolving as $(1 + z)^{1.5}$ to $z = 1.5$ (with no contribution prior to $z = 1.5$) is sufficient to reproduce
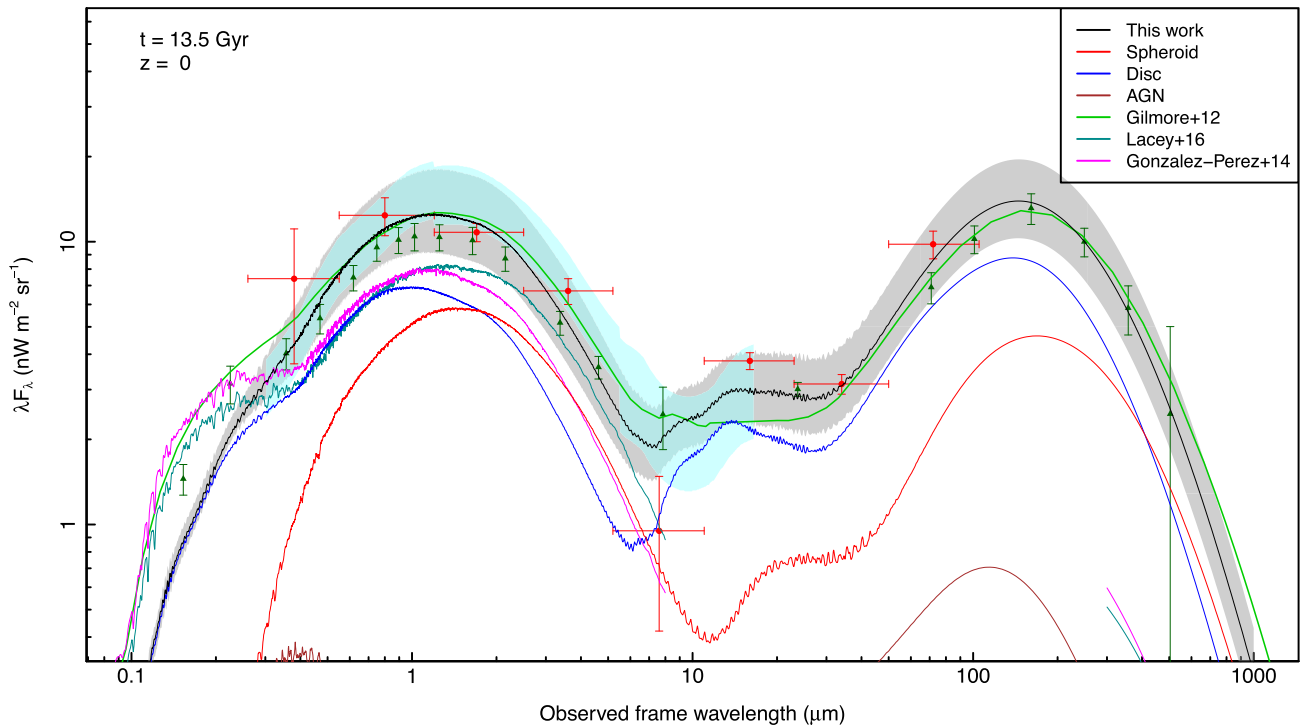

Figure 9. The IGL and EBL at $z = 0$. Black curve and band: total IGL produced by the model in Section 3 with uncertainty, blue: IGL attributed to discs, red: spheroids, brown: AGN, green: the Gilmore et al. (2012) semi-analytic model, pink: the Gonzalez-Perez et al. (2014) semi-analytic model and orange: the Lacey et al. (2016) semi-analytic model. The Driver et al. (2016c) measurements are the dark green triangles, with measurements of the EBL from of γ-ray data by Biteau & Williams (2015) the red points. The cyan region represents the 1σ constraints from H.E.S.S. Collaboration (2013).
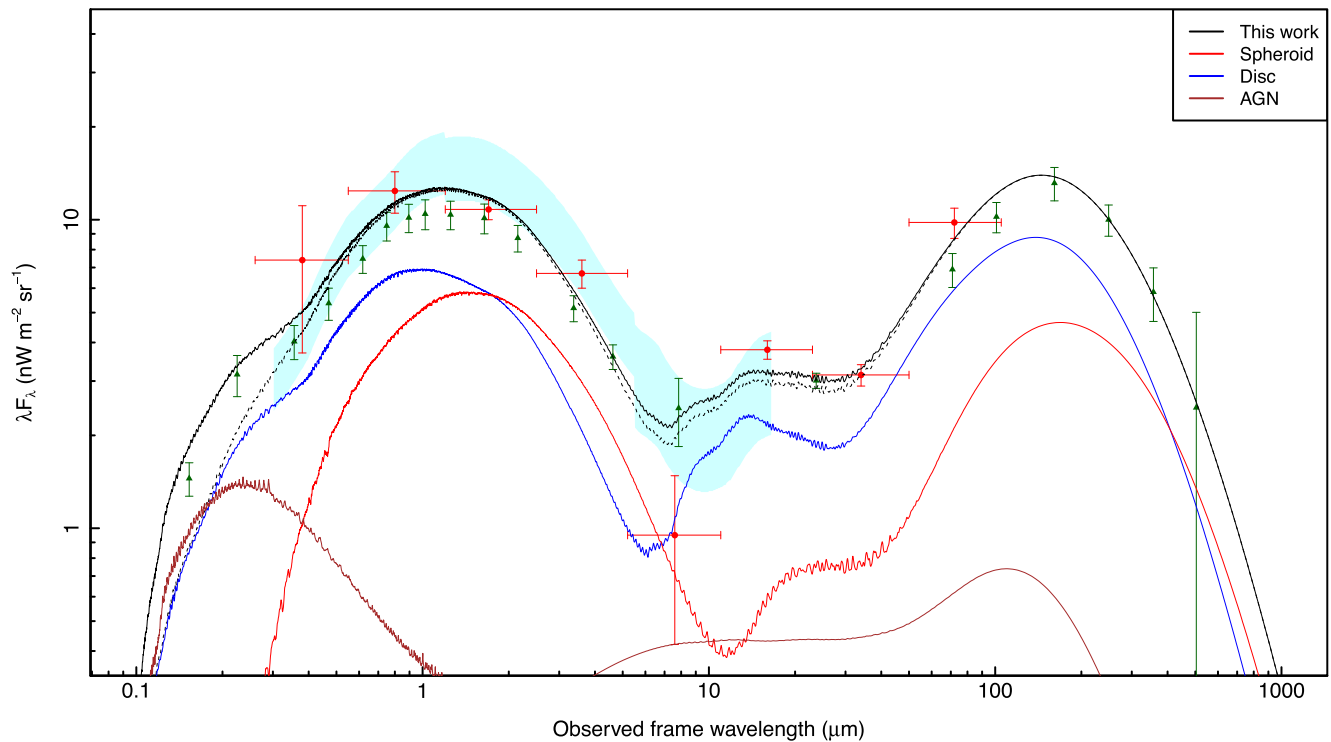
Figure 10. The IGL and EBL at $z = 0$, as in Fig. 9, with an additional component from low-level AGN. The solid black line represents the new model curve, the dashed line the model curve in Fig. 9 for comparison and brown is the enhanced AGN component.

the characteristic shape of the ultraviolet IGL. Fig. 10 shows this spectrum and demonstrates the potential role of low-level AGN activity in keeping the low-redshift Universe ionized. Further work on quantifying their contribution to the low-redshift CSED is clearly warranted.

We estimate the potential upward adjustments from incompleteness and AGN to be 0–2 nW m^{-2} sr^{-1}. Despite this, there still exists significant tension between the IGL prediction from the phenomological model and the direct Mattila et al. (2017) EBL estimate using dark cloud observations. A diffuse component to the EBL originating at low to intermediate redshifts cannot be excluded.

In the optical, the phenomological model is consistent with the γ-ray measurements of the EBL while exceeding the Driver et al. (2016c) IGL measurements. This extra light could potentially originate from stripped older stellar populations in the halo environment, however a more likely explanation is SED modelling and other forms of error inherent in the phenomological model. In the near-infrared, the phenomological model falls $\sim 1\sigma$ below the H.E.S.S. measurements. This could be tentative evidence for diffuse emission from the epoch of reionization. Most likely, this simply reflects a discrepancy between the adopted EBL model used by the γ-ray measurements. Certainly it would be very useful to recompute the H.E.S.S. and MAGIC constraints using our model.

We also compute the IGL from the mock GALFORM photometry. Here, we elect to show the raw predictions, as computed from the discrete CSEDs shown in Fig. 6. These are interpolated using a 24 point spline and summed over redshift accordingly. Where a CSED is not predicted or interpolated, i.e. shortwards of the pivot wavelength of the *GALEX* FUV filter (153.5 nm) and longwards of

870 µm, it is set to zero. As a result, the model curves show a characteristic sawtooth shape at short wavelengths due to summation over discrete time-steps.

GALFORM is able to predict the far-infrared CSED longward of 70 µm, but the corresponding predictions of the CIB and IGL depend on how the non-prediction of emission from polycyclic aromatic hydrocarbons is treated. Here, we treat them as is – therefore, performing the IGL summation will result in the predicted CIB between 8 and ∼400 µm being systematically lower than expected as the loss of flux is redshifted as shown in Fig. 9.

Unsurprisingly, both iterations of GALFORM produce a COB lower than the Driver et al. (2016c) IGL measurements. This is a consequence of the underprediction of the CSFH for $z < 3$. When adjusted for the normalization of the CSED, the Gonzalez-Perez et al. (2014) iteration of GALFORM produces predictions of the optical IGL consistent with the phenomological model and the H.E.S.S. and MAGIC TeV γ-ray EBL observations.

The Lacey et al. (2016) semi-analytic model produces significantly more radiation in the near-infrared compared to Gonzalez-Perez et al. (2014). This originates at $z > 1$ – observe the difference between the Gonzalez-Perez et al. (2014) and Lacey et al. (2016) predictions in Fig. 6. This has interesting implications for SED modelling at high redshifts, given the use of the Maraston (2005) stellar libraries in the Lacey model versus the Bruzual & Charlot (2003) libraries for all other models. On that basis, it is too early to pinpoint the exact cause of the discrepancy between the IGL and EBL in the near-infrared – one would need the total errors in both a high-redshift CSED measurement (from the combination of SED modelling, incompleteness and cosmic sample variance) and the γ-ray EBL measurements to be less than 5 per cent at any one
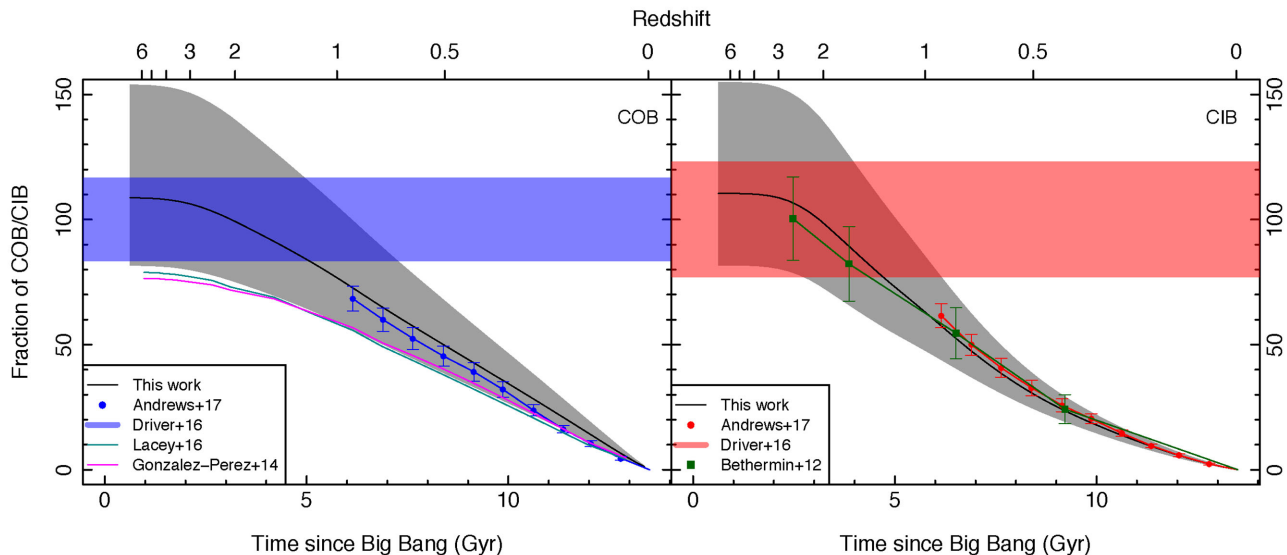
Figure 11. Contributions to the COB (left) and CIB (right) as a function of the age of the Universe relative to the total COB and CIB measured by Driver et al. (2016c), compared to measurements from Andrews et al. (2017b) and Béthermin et al. (2012a) and predictions of the COB from Gonzalez-Perez et al. (2014) and Lacey et al. (2016). Bands indicate the respective uncertainty ranges.

wavelength. In the future, increasing amounts of TeV data will lead to stronger constraints on the shape of the COB – see Biteau & Williams (2015) for an early compilation of measurements. Additionally, observations of PeV gamma-rays will lead to similar constraints on the CIB via the same method.

6.3 The cosmic optical and infrared backgrounds

We can now break down the EBL into its two key components – the COB and CIB, respectively – by integrating under the respective model curves over the relevant wavelength ranges. Given that GALFORM does not model the mid-infrared, we limit ourselves to comparing the semi-analytic model predictions with the observations in the ultraviolet to the near-infrared only.

Our model (see Fig. 11) predicts a roughly equal split between the COB and CIB, in line with observations (see Driver et al. 2016c and compilation within). We predict integrated values for the COB and CIB of $26.0^{+10.7}_{-6.5}$ and $28.0^{+11.2}_{-7.2}$ nW m^{-2} sr^{-1} respectively for the current epoch, and a peak value for the COB of $12.6^{+5.6}_{-3.4}$ nW m^{-2} sr^{-1} at 1.19 μm at the current epoch. This is in agreement with H.E.S.S. and MAGIC, which find maximum values of 15.0 ± 3.6 and $12.75^{+2.75}_{-2.29}$ nW m^{-2} sr^{-1}, respectively, both at 1.4 μm. The Gonzalez-Perez et al. (2014) iteration of GALFORM underpredicts the integrated COB by about 35 per cent, yielding an integrated value of 15.8 nW m^{-2} sr^{-1}, while the Lacey et al. (2016) model predicts 16.7 nW m^{-2} sr^{-1}. Both models also reach peak values of the COB below the H.E.S.S. and MAGIC observations – 7.7 nW m^{-2} sr^{-1} at $\lambda = 1.18$ μm and 8.0 nW m^{-2} sr^{-1} at 1.36 μm for the Gonzalez-Perez and Lacey models, respectively. For comparison, the Gilmore et al. (2012) model obtains 29.0 and 27.0 nW m^{-2} sr^{-1} for the integrated COB and CIB, respectively, and predicts a peak value of the COB of 12.7 nW m^{-2} sr^{-1} at 1.28 μm. Our model predicts an AGN contribution of approximately 0.6 nW m^{-2} sr^{-1} or 2.5 per cent (approximately equally split between obscured and unobscured AGN) to the integrated COB and 1.4 nW m^{-2} sr^{-1} or 5.1 per cent to the integrated CIB (mostly from obscured AGN).

Finally, our model predicts a CIB of $0.53^{+0.24}_{-0.15}$ nW m^{-2} sr^{-1} at 850 μm, in line with the $0.43^{+0.24}_{-0.15}$ nW m^{-2} sr^{-1} observed using galaxy number counts from SCUBA-II (Chen et al. 2013b) and $0.50^{+0.23}_{-0.19}$ nW m^{-2} sr^{-1} from direct observations using the *Cosmic Background Explorer* (Fixsen et al. 1998). The Gonzalez-Perez et al. (2014) and Lacey et al. (2016) models also show good agreement, predicting 0.44 and 0.54 nW m^{-2} sr^{-1}, respectively. The CIB at this wavelength primarily originates from galaxies at $z = 1 - 3$ (Zavala et al. 2017), lending confidence to the predictions of all models at higher redshifts.

Fig. 11 shows the accumulation of the COB and the CIB as one looks back in time. All model contributions to the CIB agree very well with both the Andrews et al. (2017b) and Béthermin et al. (2012a) measurements, while the phenomological model slightly overpredicts the COB relative to Andrews et al. (2017b). The phenomological model reaches final values of the COB and CIB fully consistent with Driver et al. (2016c). The figure also shows the underprediction of the COB by GALFORM. This is not surprising given the deficit of the GALFORM predicted CSED below the phenomological model (see Figs 5 and 6), supporting the predictions of the phenomological model.

Fig. 12 shows the advantage of CSED measurements at multiple epochs over comoving IGL measurements at $z = 0$ for constraining galaxy evolution models – the CSED measurements are able to constrain the gradient of this curve at multiple epochs, whereas the COB, CIB, IGL and EBL at these epochs is unobservable. Both our model and Gilmore et al. (2012) give similar values for the present-day IGL, COB and CIB but differ at higher redshifts. We find that the comoving COB increases monotonically with time, while the CIB peaks about 9.25 Gyr, diminishing very slowly thereafter. The total IGL initially increases rapidly, before levelling off at $\sim$51 nW m^{-2} sr^{-1} by approximately 9 Gyr. The Gilmore et al. (2012) model obtains similar predictions, with the CIB peaking at a slightly earlier time. Like all cosmic background radiation, the integrated IGL, EBL, COB and CIB will diminish over time due to redshifting if it is not maintained by further energy production pathways.
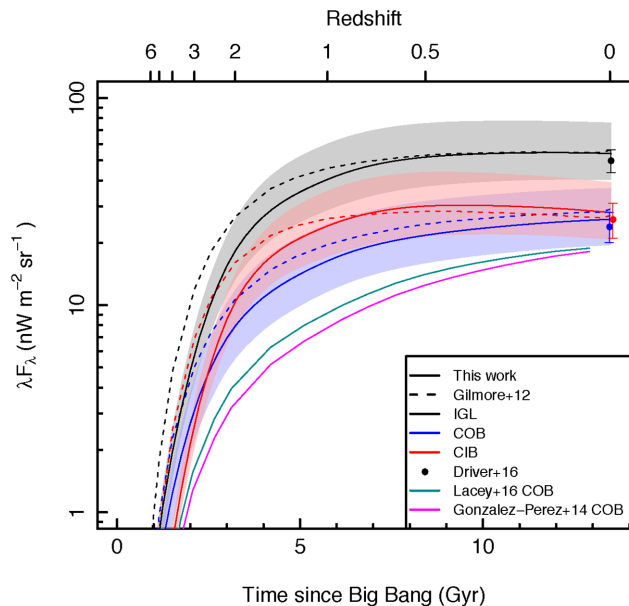
Figure 12. The comoving IGL, COB and CIB as a function of cosmic time for the phenomological model and Gilmore et al. (2012) with predictions for the COB from Gonzalez-Perez et al. (2014) and Lacey et al. (2016). The Driver et al. (2016c) measurements at $z = 0$ are shown for comparison. Bands indicate the respective model uncertainty ranges.

6.4 Stellar mass growth

While the phenomological model is focused and calibrated to energy, it is also capable of providing a complete description of stellar and dust mass evolution.

Fig. 13 shows the predicted buildup of stellar mass as a function of time for spheroids and discs (more precisely, the material that exists in spheroids and discs today). We show two curves – total stellar mass formed, computed by integrating the CSFH fitting functions (dashed lines, with bands to indicate the model uncertainty) and mass surviving at the specified time (solid lines). The curves differ as stellar material is returned to the ISM by supernovae and winds of thermally pulsating asymptotic giant branch stars. The Bruzual & Charlot (2003) models return from 35 per cent at 1 Gyr to 44 per cent at 10 Gyr of stellar mass to the ISM and place 8 per cent at 1 Gyr to 14 per cent at 10 Gyr into stellar remnants.

The green and blue points represent the total stellar mass density as reported by Moffett et al. (2016a) and Wright et al. (2017). The Moffett et al. (2016a) integrated stellar mass estimates have a 32 per cent uncertainty, equally portioned (22 per cent each) between uncertainty in the fitted functions and cosmic sample variance. The model predicts an almost equal distribution of stellar mass residing in discs (49.9 per cent) and spheroids (50.1 per cent), reproducing the 47–53 per cent stellar mass ratio of Moffett et al. (2016b). ('Little blue spheroids' are deemed to be disc material.) We do not have to adjust the spheroid star formation history by 25 per cent akin to Driver et al. (2013). Note that the spheroid to disc mass ratio is independent of cosmic variance, barring large hidden clustering effects. We also note that the total stellar mass in spheroids enters a slow decline since $t = 5$ Gyr with the total stellar mass levelling off at $t \sim 10$ Gyr, in agreement with Driver et al. (2013).

We supplement Fig. 13 with predictions derived by Guo et al. (2016) from the Gonzalez-Perez et al. (2014) version of GALFORM and the EAGLE suite of hydrodynamic simulations (Schaye et al. 2015). Briefly, the EAGLE simulation used by Guo et al. (2016)
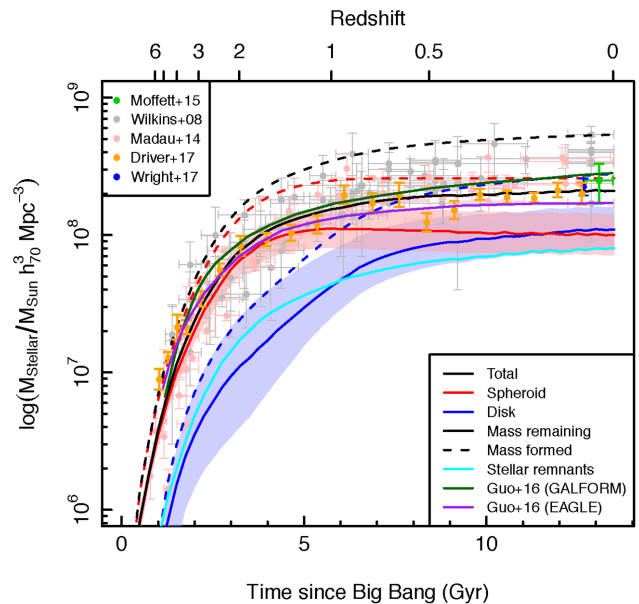

Figure 13. Stellar mass as a function of cosmic time in the empirical model, with mass formed (dashed lines) and mass surviving (solid lines, with bands to indicate the model uncertainty) for spheroids (red), discs (blue) and both combined (black). The total mass in stellar remnants for both components is shown in cyan. The green, blue and orange points represent the Moffett et al. (2016a), Wright et al. (2017) and Driver et al. (2017) stellar mass measurements, respectively, while the faint red and grey points represent the Madau & Dickinson (2014) and Wilkins, Trentham & Hopkins (2008) compilations. Also shown are predictions from GALFORM (dark green) and EAGLE (purple).

consists of a $(100 \text{ cMpc})^3$ box populated by 1504^3 particles of both gas and dark matter. EAGLE uses a Chabrier (2003) IMF and the Bruzual & Charlot (2003) stellar libraries to derive mock photometry and stellar masses. The phenomological model predicts stellar mass equally as good as GALFORM, and matches the low-redshift data better than EAGLE.

6.5 Dust mass growth

Using the phenomological model, we can also arrive at predictions of the dust mass density from the normalization constant used to scale up the Dale et al. (2014) templates to the total energy absorbed and re-released into the far-infrared. Two parameters are necessary to do so – the mass of a gas particle with respect to the mass of a hydrogen atom $m_{\text{gas}}/m_{\text{H}}$ and the dust to gas mass ratio $M_{\text{dust}}/M_{\text{gas}}$. We assume $m_{\text{gas}}/m_{\text{H}} = 1.3$ and $M_{\text{dust}}/M_{\text{gas}}$ that scales linearly with the generating function for the metallicity of newly formed stars (i.e. the total stellar mass formed, see Fig. 2) to reach $M_{\text{dust}}/M_{\text{gas}} = 10^{-2.5}$ at $z = 0$. The assumed $M_{\text{dust}}/M_{\text{gas}}$ ratio at $z = 0$ value is within the range of $M_{\text{dust}}/M_{\text{gas}}$ observed in nearby galaxies by the *Herschel* Reference Survey (Cortese et al. 2016), while $m_{\text{gas}}/m_{\text{H}} = 1.3$ is assumed by the same to account for helium in the ISM.

Fig. 14 shows these predictions compared to the Driver et al. (2017) and Dunne et al. (2011) observations, as well as GALFORM. We smooth our model predictions with a ten-point spline to remove discretization caused by the abrupt shifts in the choice of Dale et al. (2014) template spectra. For $0.45 < z < 1.75$, the fraction of the total dust mass density resulting from predictions and low-significance far-infrared observations increases with redshift (see e.g. fig. 7 of Andrews et al. 2017b). The phenomological model predicts higher
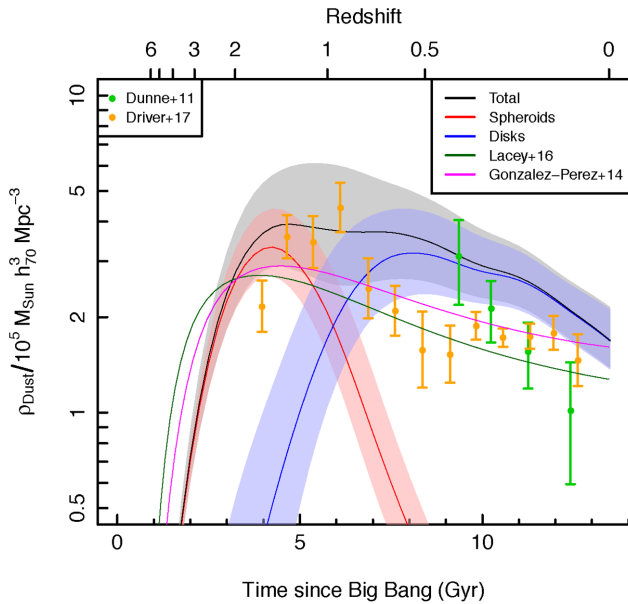
Figure 14. Dust mass density as a function of cosmic time in the empirical model, with dust mass in spheroids, discs and both combined (red, blue and black, respectively, with bands to indicate uncertainty), with observations by Dunne et al. (2011) (green) and Driver et al. (2017) (orange) and predictions from GALFORM – Gonzalez-Perez et al. (2014) in pink and Lacey et al. (2016) in dark green.

dust mass densities at low redshifts than literature measurements and GALFORM. Given the large uncertainties in the Andrews et al. (2017b) far-infrared CSEDs, the fraction of the total dust mass density arising from predictions, the underlying shallowness of the far-infrared photometry (especially at 70 μm rest frame), and the lack of a comprehensive collection of literature measurements of the dust mass density (akin to the CSFH), this overprediction is not a concern.

The phenomological model predicts that elliptical galaxies become mostly devoid of dust by 8 Gyr. This is consistent with the 76 per cent non-detection rate of elliptical galaxies in the *Herschel* Reference Survey (Smith et al. 2012) and 94.5 per cent in H-ATLAS (Rowlands et al. 2012). The small number of elliptical galaxies with detectable dust can be plausibly explained by the result of accretion from mergers with star-forming galaxies, an effect not accounted for in the phenomenological model and tentatively suggested by the observations.

7 CONCLUSION

We have extended the Driver et al. (2013) model to produce predictions of the CSED and IGL from the far-ultraviolet to the far-infrared over the life of the Universe to incorporate dust attenuation and emission from AGN. The model is based on simple expressions of the CSFH as attributed to spheroids and discs, with the spheroid star formation linked to AGN activity and dominating at high redshift. We use the Bruzual & Charlot (2003) stellar libraries, the Charlot & Fall (2000) dust attenuation prescription and the Dale et al. (2014) dust emission spectra in order to reproduce the Andrews et al. (2017b) CSED estimates at low and intermediate redshifts. We then link spheroid star formation to AGN activity and derive spectra for unobscured and obscured AGN using the vanden Berk et al. (2001) composite spectrum to derive predictions of the

CSED at high redshifts. This model is able to reproduce observations of the IGL, stellar and dust mass densities and the fractions of stellar mass in bulges and discs.

We have also obtained equivalent semi-analytic predictions of the CSED using GALFORM (Gonzalez-Perez et al. 2014; Lacey et al. 2016). We find that GALFORM is able to reproduce the shape of both the unattenuated and attenuated CSEDs well over $0 < z < 1$, but underpredicts the normalization due to underpredicting the cosmic star formation history (Mitchell et al. 2014; Guo et al. 2016; Lacey et al. 2016). GALFORM does not model the mid-infrared emission due to the lack of a prescription for emission and absorption from polycyclic aromatic hydrocarbons and underestimates the amount of dust attenuation in the ultraviolet, presumably due to galaxy half-mass radii being overpredicted on average (Merson et al. 2016).

Our model does not include a clustering prescription by design. We will examine the CSED as a function of environment using the GAMA group (Robotham et al. 2011) and large scale structure (Alpaslan et al. 2014) catalogues and their intermediate redshift equivalents in a future paper. Other considerations, such as the CSED as a function of morphology and inclination, will also be examined in future works.

The attribution of the CSFH to spheroids and discs may be verified using accurate bulge-disc decompositions of both samples where permitted by image resolution. While such a sample currently exists in GAMA at low redshift ($z < 0.06$), there are still reasonable doubts as to whether bulge-disc decomposition codes are able to converge on a physically meaningful model given an arbitrary or empty set of initial conditions (Lange et al. 2016). We are currently extending this sample out to $z < 0.1$ using data from the Kilo-Degree Survey (de Jong et al. 2015) and an improved bulge-disc decomposition algorithm (Robotham et al. 2017). Finely gridded stellar population models will increase the precision of modelling stellar phase metallicity, with the caveat that additional discretization and interpolation effects may arise from coarseness in the underlying isochrones. Deeper far-infrared data, especially 70 μm, is required to derive firm measurements on the far-infrared CSED, rigorously optimise fitting of template spectra to the measurements and derive corresponding predictions of dust temperature distributions. The incorporation of AGN templates into MAGPHYS, a reduction of SED modelling error, cosmic sample variance and incompleteness by a factor of about 4 each precise measurements of the CSED at higher redshifts and are all required to derive strong constraints on the contribution of AGN to the CSED, the contribution of diffuse emission to the (total) CSED and EBL and the shape and normalization of the near-infrared IGL and EBL.

In the future, radio data from the Australian Square Kilometre Array Pathfinder, *Spektr-RG*'s eROSITA and the COSMOS HI Large Extragalactic Survey will become available for the GAMA and G10/COSMOS regions. This data, in combination with future improvements to SED fitting tools to accommodate the expanded wavelength range, will increase our understanding of the gas content and AGN activity and hence allow us to extend our models and measurements of the CSED and IGL to radio wavelengths. In addition, the Wide Area VISTA Extragalactic Survey (Driver et al. 2016a) will reduce the errors associated with cosmic sample variance and incompleteness in the empirical CSED measurements. Data from the Cherenkov Telescope Array will help reduce the systematic error inherent in the γ-ray EBL measurements. Finally, the *James Webb Space Telescope*, *Wide-Field Infrared Space Telescope* and *Euclid* will allow investigations at higher redshift, thus fully constraining the optical and near-infrared CSED across the entire history of the Universe.

REFERENCES

Ahnen M. L. et al., 2016, A&A, 590, A24
Allard F., Hauschildt P. H., 1995, ApJ, 445, 433
Alpaslan M. et al., 2014, MNRAS, 438, 177
Andrews S. K., Driver S. P., Davies L. J. M., Kafle P. R., Robotham A. S. G., Wright A. H., 2017a, MNRAS, 464, 1569
Andrews S. K. et al., 2017b, MNRAS, 470, 1342
Baldry I. K., Glazebrook K., 2003, ApJ, 593, 258
Bernstein R., Freedman W. L., Madore B. F., 2002, ApJ, 571, 56
Berta S. et al., 2011, A&A, 532, A49
Béthermin M. et al., 2012a, A&A, 542, A58
Béthermin M. et al., 2012b, ApJ, 757, L23
Béthermin M. et al., 2014, A&A, 567, A103
Biteau J., Williams D. A., 2015, ApJ, 812, 60
Bourne N. et al., 2017, MNRAS, 467, 1360
Bruzual G., 2007, in Vallenari A., Tantalo R., Portinari L., Morettieds A., eds, ASP Conf. Ser. Vol. 374, From Stars to Galaxies: Building the Pieces to Build Up the Universe. Astron. Soc. Pac., San Francisco, p. 303
Bruzual G., Charlot S., 2003, MNRAS, 344, 1000
Bruzual G., Charlot S., González Lópezlira R., Srinivasan S., Boyer M. L., Riebel D., 2013, in Thomas D., Pasquali A., Ferreras I., eds, Proc. IAU Symp. No. 295, The LF of TP-AGB Stars in the LMC/SMC. Cambridge Univ. Press, Cambridge, p. 282
Buchner J. et al., 2015, ApJ, 802, 89
Burgarella D. et al., 2013, A&A, 554, A70
Calzetti D., Armus L., Bohlin R. C., Kinney A. L., Koornneef J., Storchi-Bergmann T., 2000, ApJ, 533, 682
Capak P. et al., 2015, Nature, 522, 455
Capozzi D., Maraston C., Daddi E., Renzini A., Strazzullo V., Gobat R., 2016, MNRAS, 456, 790
Cardelli J. A., Clayton G. C., Mathis J. S., 1989, ApJ, 345, 245
Carniani S. et al., 2015, A&A, 584, A78
Chabrier G., 2003, PASP, 115, 763
Charlot S., Fall S. M., 2000, ApJ, 539, 718
Chary R., Elbaz D., 2001, ApJ, 556, 562
Chen C.-T. J. et al., 2013a, ApJ, 773, 3
Chen C.-C., Cowie L. L., Barger A. J., Casey C. M., Lee N., Sanders D. B., Wang W.-H., Williams J. P., 2013b, ApJ, 776, 131
Conroy C., Gunn J. E., 2010, ApJ, 712, 833
Cortese L. et al., 2016, MNRAS, 459, 3574
Cowley W. I., Béthermin M., Lagos C. d. P., Lacey C. G., Baugh C. M., Cole S., 2017, MNRAS, 467, 1231
Cucciati O. et al., 2012, A&A, 539, A31
da Cunha E., Charlot S., Elbaz D., 2008, MNRAS, 388, 1595
Dale D., Helou G., 2002, ApJ, 576, 159
Dale D., Helou G., Magdis G. E., Armus L., Díaz-Santos T., Shi Y., 2014, ApJ, 784, 83
Davies L. J. M. et al., 2015, MNRAS, 447, 1014
Davies L. J. M. et al., 2016, MNRAS, 461, 458
de Jong J. T. A. et al., 2015, A&A, 582, A62
Dole H. et al., 2009, A&A, 451, 417
Domínguez A. et al., 2011, MNRAS, 410, 2556
Draine B. T., Li A., 2007, ApJ, 657, 810
Driver S. P., Popescu C. C., Tuffs R. J., Graham A. W., Liske J., Baldry I. K., 2008, ApJ, 678, L101
Driver S. P. et al., 2011, MNRAS, 413, 971
Driver S. P. et al., 2012, MNRAS, 427, 3244
Driver S. P., Robotham A. S. G., Bland-Hawthorn J., Brown M., Hopkins A., Liske J., Phillipps S., Wilkins S., 2013, MNRAS, 430, 2622
Driver S. P., Davies L. J., Meyer M., Power C., Robotham A. S. G., Baldry I. K., Liske J., Norberg P., 2016a, in Skillen I., Balcells M., Trager S., eds, Multi-Object Spectroscopy in the Next Decade: Big Questions, Large Surveys, and Wide Fields. Astron. Soc. Pac., San Francisco, p. 269
Driver S. P. et al., 2016b, MNRAS, 455, 3911
Driver S. P. et al., 2016c, ApJ, 827, 108
Driver S. P. et al., 2017, MNRAS, in press
Dunne L. et al., 2011, MNRAS, 417, 1510
Dwek E. et al., 1998, ApJ, 508, 106
Elvis M. et al., 1994, ApJS, 95, 1
Erb D., Shapley A., Pettini M., Steidel C. C., Reddy N. A., Adelberger K. L., 2006, ApJ, 644, 813
Finke J. D., Razzaque S., Dermer C. D., 2010, ApJ, 712, 238
Fixsen D. J., Dwek E., Mather J. C., Bennett C. L., Shafer R. A., 1998, ApJ, 508, 123
Franceschini A., Rodighiero G., Vaccari M., 2008, A&A, 487, 837
Gallazzi A., Brinchmann J., Charlot S., White S. D. M., 2009, MNRAS, 383, 1439
Gebhardt K. et al., 2000, AJ, 119, 1157
Gil de Paz A. et al., 2005, ApJ, 627, L29
Gilmore R. C., Somerville R. S., Primack J. R., Domínguez A., 2012, MNRAS, 422, 3189
González Delgado R. M. et al., 2015, A&A, 581, A103
Gonzalez-Perez V., Lacey C. G. Baugh C. M., Lagos C. D. P., Helly J., Campbell D. J. R., Mitchell P. D., 2014, MNRAS, 439, 264
Gonzalez-Perez V. et al., 2017, MNRAS, submitted
Gordon K. D., Clayton G. C., Misselt K. A., Landolt A. U., Wolff M. J., 2003, ApJ, 594, 279
Graham A. W., Scott N., 2015, ApJ, 798, 54
Guo Q. et al., 2016, MNRAS, 461, 3457
Hauser M. G. et al., 1998, ApJ, 508, 25
H.E.S.S. Collaboration, 2015 A&A, 550, A4
Hopkins A. M., Beacom J. F., 2006, ApJ, 651, 142
Ibarra-Medel H. J. et al., 2016, MNRAS, 463, 2799
Inoue Y., Inoue S., Kobayashi M. A. R., Makiya R., Niino Y., Totani T., 2013, ApJ, 768, 197
Jauzac M. et al., 2011, A&A, 525, A52
Kawara K. et al., 2017, PASJ, 69, 31
Keenan R. C., Barger A. J., Cowie L. L., Wang W.-H., 2010, ApJ, 723, 40
Kelvin L. S. et al., 2014, MNRAS, 439, 1245
Kennicutt R. C., 1983, ApJ, 272, 54
Kennicutt R. C., 1998, ApJ, 498, 541
Khaire V., Srianand R., 2015, ApJ, 805, 33
Kormendy J., Ho L. C., 2013, ARA&A, 51, 511
Kroupa P., 2001, MNRAS, 322, 231
Lacey C. et al., 2016, MNRAS, 462, 3854
Lagos C. d. P., Baugh C. M., Zwaan M. A., Lacey C. G., Gonzalez-Perez V., Power C., Swinbank A. M., van Kampen E., 2014, MNRAS, 440, 920
Lange R. et al., 2016, MNRAS, 462, 1470
Le Borgne D., Rocca-Volmerange B., Prugniel P., Lançon A., Fioc M., Soubiran C., 2004, A&A, 425, 881
Levenson L. R., Wright E. L., 2008, ApJ, 683, 585
Lilly S. J., Le Fevre O., Hammer F., Crampton D., 1996, ApJ, 460, L1
Liske J. et al., 2015, MNRAS, 452, 2087
Lusso E. et al., 2013, ApJ, 777, 86
Madau P., Dickinson M., 2014, ARA&A, 52, 415
Madau P., Pozzetti L., 2000, MNRAS, 312, L9
Magorrian J. et al., 1998, AJ, 115, 2285
Maraston C., 2005, MNRAS, 362, 799
Maraston C., Daddi E., Renzini A., Cimatti A., Dickinson M., Papovich C., Pasquali A., Pirzkal N., 2006, ApJ, 652, 82
Marsden G. et al., 2009, ApJ, 707, 1729
Matsumoto T. et al., 2005, ApJ, 626, 31
Matsumoto T., Kim M. G., Pyo J., Tsumura K., 2015, ApJ, 807, 57
Matsuoka Y., Ienaka N., Kawara K., Oyabu S., 2011, ApJ, 736, 119

Matsuura S. et al., 2017, ApJ, 839, 7

Mattila K., Väisänen P., Lehtinen K., von Appen-Schnur G., Leinert C., 2017, MNRAS, 470, 2152

McAlpine K., Jarvis M. J., Bonfield D. G., 2013, A&A, 544, A156

McDermid R. M. et al., 2015, MNRAS, 448, 3484

Ménard B., Fukugita M., 2012, ApJ, 754, 116

Merson A. I., Baugh C. M., Gonzalez-Perez V., Abdalla F. B., Lagos C. d. P., Mei S., 2016, MNRAS, 456, 1681

Meurer G. R., Heckman T. M., Calzetti D., 1999, ApJ, 521, 64

Mitchell P. D., Lacey C. G., Cole S., Baugh C. M., 2014, MNRAS, 444, 2637

Moffett A. J. et al., 2016a, MNRAS, 457, 1308

Moffett A. J. et al., 2016b, MNRAS, 462, 4336

Mullaney J. R. et al., 2012a, MNRAS, 419, 9

Mullaney J. R. et al., 2012b, ApJ, 753, L30

Noël N. E. D., Greggio L., Renzini A., Carollo C. M., Maraston C., 2013, ApJ, 772, 58

Padovani P., Bonzini M., Kellermann K. I., Miller N., Mainieri V., Tozzi P., 2015, MNRAS, 452, 1263

Palanque-Delabrouille N. et al., 2016, A&A, 587, A41

Partridge R. B., Peebles P. J. E., 1967a, ApJ, 147, 868

Partridge R. B., Peebles P. J. E., 1967b, ApJ, 148, 377

Prugniel P., Soubiran C., 2001, A&A, 369, 1048

Puget J.-L., Abergel A., Bernard J.-P., Boulanger F., Burton W. B., Desert F.-X., Hartmann D., 1996, A&A, 308, L5

Richards G. et al., 2006, AJ, 131, 2766

Rieke G. H., Alonso-Herrero A., Weiner B. J., Pérez-González P. G., Blaylock M., Donley J. L., Marcillac D., 2009, ApJ, 692, 556

Robotham A. S. G. et al., 2011, MNRAS, 416, 2640

Robotham A. S. G. et al., 2014, MNRAS, 444, 3986

Robotham A. S. G., Taranu D. S., Tobar R., Moffett A., Driver S. P., 2017, MNRAS, 466, 1513

Rodighiero G. et al., 2015, ApJ, 800, L10

Rosario D. J. et al., 2012, A&A, 545, A45

Rowlands K. et al., 2012, MNRAS, 419, 2545

Savage B. D., Mathis J. S., 1979, ARA&A, 17, 73

Schaye J. et al., 2015, MNRAS, 446, 521

Scoville N. et al., 2007, ApJS, 172, 1

Siebenmorgen R., Heymann F., Efstathiou A., 2015, A&A, 583, A180

Silk J., Rees M. J., 1998, A&A, 331, L1

Smith M. W. L. et al., 2012, ApJ, 748, 123

Smolčić V. et al., 2009, ApJ, 696, 24

Somerville R. S., Hopkins P. F., Cox T. J., Robertson B. E., Hernquist L., 2008, MNRAS, 391, 481

Somerville R. S., Gilmore R. C., Primack J. R., Domínguez A., 2012, MNRAS, 423, 1992

Springel V. et al, 2005, Nature, 435, 629

Stanley F., Harrison C. M., Alexander D. M., Swinbank A. M., Aird J. A., Del Moro A., Hickox R. C., Mullaney J. R., 2015, MNRAS, 453, 591

Symeonidis M. et al., 2013, MNRAS, 431, 2317

Taylor E. N. et al., 2011, MNRAS, 418, 1587

Thilker D. A. et al., 2007, ApJS, 173, 538

Totani T., Yoshii Y., Iwamuro F., Maihara T., Motohara K., 2001, ApJ, 550, L137

Tremonti C. A. et al., 2004, ApJ, 613, 898

Triester E., Urry C. M., 2006, ApJ, 652, L79

Ueda Y., Akiyama M., Hasinger G., Miyaji T., Watson M. G., 2014, ApJ, 786, 104

vanden Berk D. E. et al., 2001, AJ, 122, 549

Viero M. P. et al., 2013, ApJ, 779, 32

Wilkins S. M., Trentham N., Hopkins A. M., 2008, MNRAS, 385, 687

Wright A. H. et al., 2016, MNRAS, 460, 765

Wright A. H. et al., 2017, MNRAS, 470, 283

Xu C. et al., 2005, ApJ, 619, L11

Zahid H. J., Kewley L. J., Bresolin F., 2011, ApJ, 730, 137

Zavala J. A. et al., 2017, MNRAS, 464, 3369

Zemcov M., Immel P., Nguyen C., Cooray A., Lisse C. M., Poppe A. R., 2017, Nat. Commun., 8, 15003

Zubko V., Dwek E., Arendt R. G., 2004, ApJS, 152, 211

SUPPORTING INFORMATION

Supplementary data are available at *MNRAS* online.

Animated versions of Figs 5 (mucsed.gif) and 6 (mfcsed.gif) are available online as supporting information. These animations also include a comparison to the Driver et al. (2012) CSED measurements (discs: orange points, spheroids: brown points).

Please note: Oxford University Press is not responsible for the content or functionality of any supporting materials supplied by the authors. Any queries (other than missing material) should be directed to the corresponding author for the article.

This paper has been typeset from a TEX/LATEX file prepared by the author.